Contrib Mineral Petrol (2013) 166:1655–1675
DOI 10.1007/s00410-013-0947-5

ORIGINAL PAPER

Metamorphic CO_2 production from calc-silicate rocks via garnet-forming reactions in the CFAS–H_2O–CO_2 system

Chiara Groppo · Franco Rolfo · Daniele Castelli · James A. D. Connolly

Received: 11 June 2013 / Accepted: 1 October 2013 / Published online: 19 October 2013
© Springer-Verlag Berlin Heidelberg 2013

Abstract The type and kinetics of metamorphic CO_2-producing processes in metacarbonate rocks is of importance to understand the nature and magnitude of orogenic CO_2 cycle. This paper focuses on CO_2 production by garnet-forming reactions occurring in calc-silicate rocks. Phase equilibria in the CaO–FeO–Al_2O_3–SiO_2–CO_2–H_2O (CFAS–CO_2–H_2O) system are investigated using *P*–*T* phase diagrams at fixed fluid composition, isobaric *T*–*X*(CO_2) phase diagram sections and phase diagram projections in which fluid composition is unconstrained. The relevance of the CFAS–CO_2–H_2O garnet-bearing equilibria during metamorphic evolution of calc-silicate rocks is discussed in the light of the observed microstructures and measured mineral compositions in two representative samples of calc-silicate rocks from eastern Nepal Himalaya. The results of this study demonstrate that calc-silicate rocks may act as a significant CO_2 source during prograde heating and/or early decompression. However, if the system remains closed, fluid–rock interactions may induce hydration of the calc-silicate assemblages and the in situ precipitation of graphite. The interplay between these two contrasting processes (production of CO_2-rich fluids vs. carbon sequestration through graphite precipitation) must be considered when dealing with a global estimate of the role exerted by decarbonation processes on the orogenic CO_2 cycle.

Keywords Orogenic CO_2 cycle · Decarbonation processes · Calc-silicate rocks · Mixed-volatile phase diagram projections · Graphite · Himalaya

Communicated by J. L. R. Touret.

Electronic supplementary material The online version of this article (doi:10.1007/s00410-013-0947-5) contains supplementary material, which is available to authorized users.

C. Groppo (✉) · F. Rolfo · D. Castelli
Department of Earth Sciences, University of Torino, Via Valperga Caluso 35, 10125 Turin, Italy
e-mail: chiara.groppo@unito.it

F. Rolfo · D. Castelli
IGG-CNR, Via Valperga Caluso 35, 10125 Turin, Italy

J. A. D. Connolly
Department of Earth Sciences, Institute of Geochemistry and Petrology, ETH Zurich, 8092 Zurich, Switzerland

Introduction

Metamorphic degassing from active collisional orogens supplies a significant amount of CO_2 to the atmosphere, playing a fundamental role in the long-term (>1 Ma) global carbon cycle (e.g. Kerrick and Caldeira 1993; Selverstone and Gutzler 1993; Bickle 1996; Berner 1999; Gaillardet and Galy 2008; Evans 2011). Primary geologic settings for the production of metamorphic CO_2 include, among others, collisional contexts where decarbonation reactions occur, at relatively high temperatures, within carbonate-bearing metasediments (i.e. calc-silicate rocks and impure marbles). Large metamorphic CO_2 fluxes should be facilitated by rapid metamorphism, at relatively high temperatures, of large volumes of metacarbonate rocks coupled with facile escape of CO_2 to the Earth's surface (Kerrick and Caldeira 1993). The type and kinetics of metamorphic CO_2-producing processes in metacarbonate rocks is therefore of importance to understand the nature and magnitude of orogenic CO_2 cycle (e.g. Berner and Lasaga 1989; Ague 2000; Gaillardet and Galy 2008; Evans 2011; Skelton 2011).

Calc-silicate rocks are common constituents of high-grade metasedimentary sequences. Although less studied

than metapelitic and basic lithologies, the importance of calc-silicate assemblages for the reconstruction of the pressure–temperature–fluid composition evolution (P–T–X^{fluid}) of metamorphic terrains is widely recognized (e.g. Warren et al. 1987; Harley and Buick 1992; Dasgupta 1993; Fitzsimons and Harley 1994; Sengupta et al. 1997; Stephenson and Cook 1997; Buick et al. 1998). The majority of studied calc-silicate rocks come from granulite–facies terrains and are characterized by peak assemblages consisting of wollastonite + scapolite, with grossular-rich garnet often occurring as retrograde coronas (e.g. Eastern Ghats, India: Dasgupta 1993; Bhowmik et al. 1995; Sengupta et al. 1997; Sengupta and Raith 2002; Dasgupta and Pal 2005; Rauer Group and Prince Charles Mountains, East Antarctica: Harley and Buick 1992; Buick et al. 1993; Fitzsimons and Harley 1994; Stephenson and Cook 1997). In these rocks, textures, thermobarometry and phase equilibria modelling are generally consistent with the formation of grossular-rich garnet during cooling, through CASV (CaO–Al_2O_3–SiO_2–CO_2) reactions that generate CO_2-rich fluid. Therefore, it has been argued that wollastonite + scapolite-bearing calc-silicate rocks act as CO_2 source during garnet formation (e.g. Harley and Buick 1992; Harley et al. 1994; Sengupta et al. 1997).

Reaction textures in calc-silicate rocks are usually interpreted using activity-adjusted T–$X(CO_2)$ sections in the simplified CASV system. This interpretation implicitly assumes that FeO and MgO components only have the effect of lowering the grossular activity in garnet, although many authors have provided evidence that clinopyroxene is an essential reactant consumed during garnet growth (e.g. Harley and Buick 1992; Dasgupta 1993; Fitzsimons and Harley 1994; Bhowmik et al. 1995; Sengupta et al. 1997). Recently, calc-silicates phase diagram topologies in the more complex CaO–FeO–Al_2O_3–SiO_2–CO_2 (CFAS–CO_2) system have been considered. Sengupta and Raith (2002) proposed a petrogenetic grid for the CFAS–CO_2 system involving clinopyroxene and discussed the effects of additional components such as MgO, Na_2O, Fe_2O_3 and H_2O. Moreover, they demonstrated the potential of garnet composition as a monitor of the P–T–X^{fluid} regime in granulite-facies rocks and stressed the need to consider garnet solid solution for a proper interpretation of the reaction textures in calc-silicate rocks (see also Kerrick 1974). Dasgupta and Pal (2005) extended the discussion to the oxidized system CFAS–CO_2–O_2, discussing the influence of T and fO_2 in the formation of grandite garnet. In both cases, the discussion was limited to high-grade calc-silicate rocks that are devoid of OH-bearing minerals.

Calc-silicate rocks often occur as layers or boudins within metapelitic granulites; therefore, significant H_2O influx from the hosting metapelites is expected during prograde metamorphism. Using numerical models, Ague (2000) showed that prograde dehydration of metapelites is able to drive decarbonation reactions in the associated metacarbonate layers, forcing the CO_2 release also during decompression and cooling, especially if metapelites dominate over calc-silicate layers. It follows that the CFAS–CO_2 model system is not necessarily adequate to model decarbonation during metamorphism and that the more complex CFAS–CO_2–H_2O system should be considered.

Following this rationale, we investigate the garnet-producing reactions in the CFAS–CO_2–H_2O system, with application to the high-grade, Grt + Cpx + Pl + Qtz calc-silicate rocks from the Main Central Thrust Zone of eastern Nepal Himalaya. The widespread occurrence of relict zoisite in the studied samples attests to the importance of the H_2O component during their metamorphic evolution. P–T grids calculated at fixed $X(CO_2)$ values show that hydrous phases are stabilized at $T < 800$ °C (see also Gordon and Greenwood 1971 for the simplified CAS–H_2O–CO_2 system). For low $X(CO_2)$ values, in particular, the zoisite stability field is progressively enlarged at the expenses of the calcite + anorthite assemblage, until the garnet-bearing reaction curves enter the zoisite stability field. At these low $X(CO_2)$ values, zoisite can thus participate in garnet-forming reactions. The CFAS–CO_2–H_2O equilibria involving garnet (grossular-almandine solid solution), zoisite, clinopyroxene, anorthite, quartz and calcite are here investigated using activity-corrected (1) P–T phase diagrams at fixed fluid composition, (2) isobaric T–$X(CO_2)$ phase diagram sections and (3) phase diagram projections in which fluid composition is not explicitly constrained.

The relevance of the CFAS–CO_2–H_2O garnet-bearing equilibria during metamorphic evolution of calc-silicate rocks is discussed in the light of the observed microstructures and measured mineral compositions in two representative calc-silicate samples. Our results: (1) define the P–T–X^{fluid} regime during the metamorphic evolution of the studied calc-silicate rocks; (2) confirm the importance of garnet composition as a monitor of the metamorphic reactions experienced by calc-silicate rocks and for the correct interpretation of reaction textures (see Sengupta and Raith 2002); (3) demonstrate that, for suitable calc-silicate bulk rock compositions, CO_2-rich C–O–H fluid can be released through garnet-producing reactions and that the amount of CO_2 released during garnet growth increases with the increase in grossular component of garnet; (4) discuss the complex interplay between two contrasting processes—i.e. the production of CO_2-rich fluids versus carbon sequestration through graphite precipitation.

Geological setting and field occurrences

Two samples of calc-silicate rocks from the upper structural levels of the Main Central Thrust Zone (MCTZ),

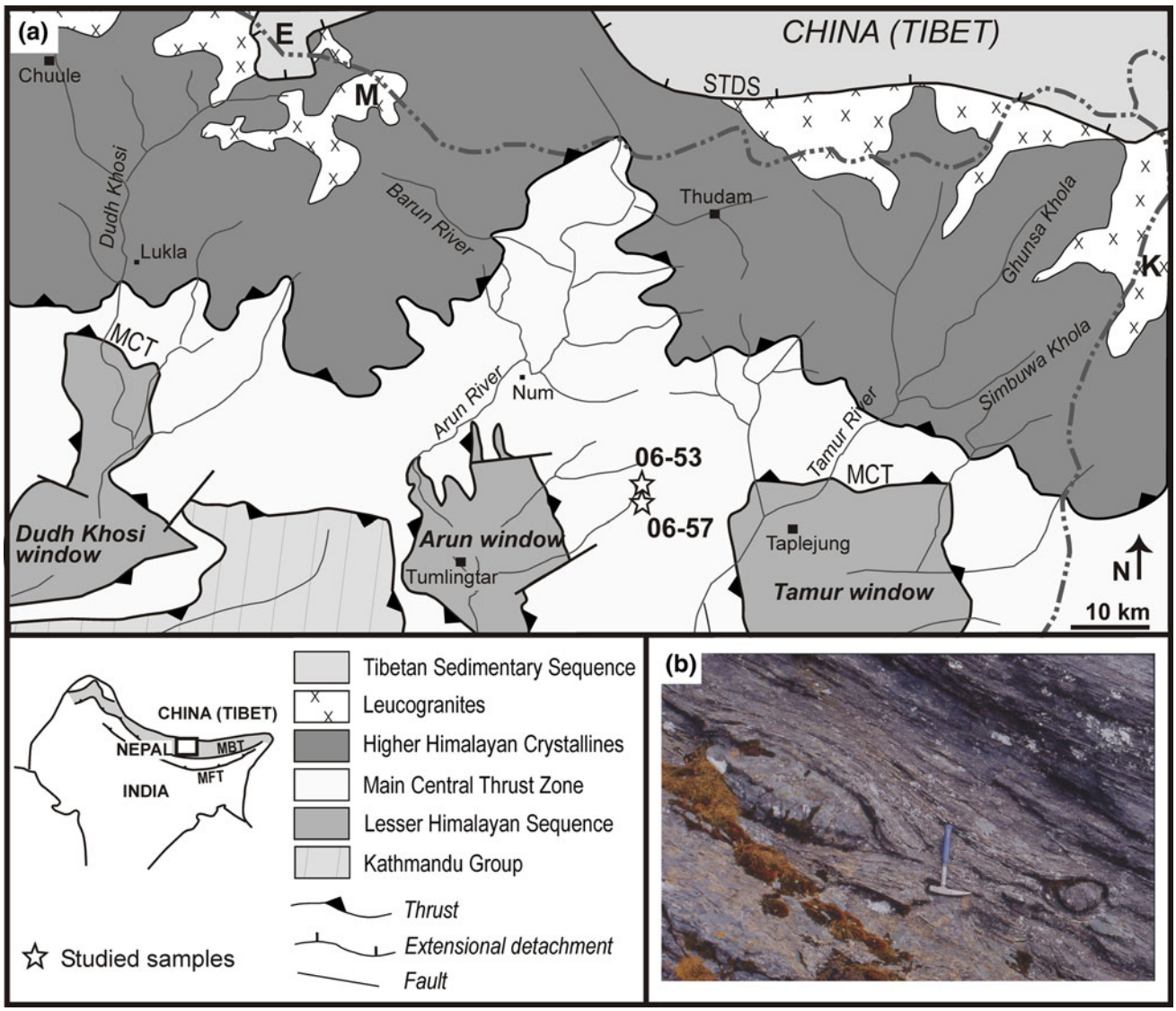

Fig. 1 **a** Simplified geological map of the central-eastern sector of the Himalayan belt (modified from Goscombe et al. 2006; Mosca et al. 2011 and Groppo et al. 2013) showing sample locations (*white stars*). The *double-dashed line* is the approximate political boundary between Nepal to the south-west, China (Tibet) to the north, India (Sikkim) to the east. *MCT* Main Central Thrust, *STDS* South Tibetan Detachment System, *E* Everest, *K* Kangchenjunga, *M* Makalu. *Inset* shows the location of the study area (*black rectangle*) in the framework of the Himalayan chain. The *grey shaded* belt approximates the location of the Higher Himalayan Crystallines. *MFT* Main Frontal Thrust, *MBT* Main Boundary Thrust. **b** Field occurrence of the studied calc-silicate rocks, forming metric boudins within the hosting anatectic paragneiss

eastern Nepal Himalaya, have been studied in detail. The samples were collected along the Milke Danda ridge, on the eastern side of the Arun Tectonic Window (Fig. 1a). In this sector of the Nepalese Himalaya, the MCTZ is well exposed and consists of a strongly deformed metapelitic sequence, with subordinate intercalations of orthogneiss, calc-silicate rocks and amphibolite, gently dipping to the NE and showing an increase in metamorphic grade upward from the garnet-biotite to the sillimanite zone (i.e. the well-known Inverted Metamorphic Sequence, see Goscombe et al. 2006 and Searle et al. 2008 for a review). In the upper portion of the MCTZ, the metapelitic sequence shows widespread evidence of anatexis (see also Groppo et al. 2010; Mosca et al. 2012) and mainly consists of Grt + Kfs + Bt + Ky ± Sil gneisses in which garnet and K-feldspar represent peritectic products of de-hydration melting reactions involving both muscovite and biotite. Peak *P–T* conditions of 780–800 °C, 10.5–11.0 kbar followed by decompression to ca. 8.5–9.0 kbar associated with moderate cooling to ca. 750 °C have been estimated by Groppo et al. (2009) from *P–T* phase diagram sections.

These anatectic gneisses host layers and boudins of calc-silicate rocks, ranging in thickness from few centimetres to some metres. The boudins are enveloped by the main foliation of the hosting gneiss and appear as massive, competent rocks within a more ductile deformed matrix (Fig. 1b). At the outcrop scale, the transition between the calc-silicate rocks and the hosting paragneiss is generally sharp, also due to the contrast in competencies between the two lithologies. A banded structure is locally observed. Marbles layers have never been observed in association with these calc-silicate rocks. Samples 06-53 and 06-57 were collected at Gidde Danda (N27°26′40.4″ E87°27′07.8″; 3,560 m a.s.l.) and in the surroundings of Ilee (N27°23′54.1″ E87°26′59.4″; 3,500 m a.s.l.), respectively (Fig. 1a).

Methods

Micro-X-ray fluorescence (μ-XRF) maps

The micro-XRF maps of the whole thin sections were acquired using a μ-XRF Eagle III-XPL spectrometer equipped with an EDS Si(Li) detector and with an Edax Vision32 microanalytical system (Department of Earth Sciences, University of Torino, Italy). The operating conditions were as follows: 100 ms counting time, 40 kV accelerating voltage and a probe current of 900 μA. A spatial resolution of about 65 μm in both x and y directions was used. Quantitative modal percentages of each mineral have been obtained by processing the μ-XRF maps with the software program "Petromod" (Cossio et al. 2002).

Mineral chemistry

Minerals were analysed with a Cambridge Stereoscan 360 SEM equipped with an EDS Energy 200 and a Pentafet detector (Oxford Instruments) at the Department of Earth Sciences, University of Torino. The operating conditions were as follows: 50 s counting time and 15 kV accelerating voltage. SEM–EDS quantitative data (spot size = 2 μm) were acquired and processed using the Microanalysis Suite Issue 12, INCA Suite version 4.01; natural mineral standards were used to calibrate the raw data; the $\Phi\rho Z$ correction (Pouchou and Pichoir 1988) was applied. Absolute error is 1 σ for all calculated oxides. Mineral chemical data of representative minerals are reported in Fig. 5 and Tables SM1-SM4. Note that in the garnet compositional notation, the Grs content actually refers to the calculated Grs+Andr sum, where Andr <5 in all the analysed garnets independently from the garnet microstructural position.

Phase diagrams computation

Phase diagrams for the CFAS–CO_2–H_2O system were calculated using Perple_X (version 6.6.6, Connolly 1990, 2009) and the thermodynamic dataset and equation of state for H_2O–CO_2 fluid of Holland and Powell (1998, revised 2004). The following solid end-members were considered in the calculation: grossular, almandine, zoisite, hedenbergite, anorthite, quartz and calcite, in addition to the solution models of garnet (Holland and Powell 1998) and binary H_2O–CO_2 fluid (Connolly and Trommsdorff 1991).

Petrography, mineral chemistry and bulk compositions

Petrography and microstructural features of the studied samples are reported in Figs. 2, 3, 4; representative compositions of the main mineral phases are given in Fig. 5 and in the Supplementary Material (Tables SM1-4).

Sample 06-57

Sample 06-57 is a medium-grained calc-silicate granofels consisting of cm-thick alternated layers differing in mineral modes and compositions, hereafter referred to as layer A (Grt-rich, Cpx-poor) and layer B (Cpx-rich, Grt-poor) (Fig. 2). The transition between the two layers is gradual.

Layer A Layer A consists of garnet (41 vol%), quartz (33 vol%), plagioclase (18 vol%), clinopyroxene (6 vol%), graphite (ca. 1 vol%) and minor zoisite. Garnet occurs in two different microstructural forms: (1) as large porphyroblasts (up to 500 μm in diameter) with a typical spongy appearance, intimately intergrown with quartz and locally partially replacing clinopyroxene at its rim (Fig. 3a, b); (2) as smaller idioblasts (ca. 50 μm in size) associated with plagioclase. In both cases, the garnet is grossular-rich (Fig. 5b), but the large porphyroblasts shows a wider range of compositions ($Alm_{19–27}Prp_{0–3}Grs_{67–74}Sps_{5–7}$) with respect to the small idioblasts associated with plagioclase ($Alm_{20–23}Prp_{1–3}Grs_{68–73}Sps_{5–6}$). Plagioclase is concentrated in the garnet-poor domains and it is an almost pure anorthite ($An_{95–97}$) (Fig. 5c); it is locally replaced along fractures by late clay minerals. Clinopyroxene occurs as medium-grained, slightly zoned, granoblasts, locally partially replaced by garnet and altered to a later kaolinite + smectite mixture along cleavages and at grain rims. Clinopyroxene cores are more rich in Mg and Al than the rims (X_{Mg} = 0.46–0.56, Al = 0.03–0.06 a.p.f.u. vs. X_{Mg} = 0.37–0.44, Al = 0.02–0.03 a.p.f.u.). Graphite is abundant (Fig. 3b) and occurs as large flakes concentrated in the plagioclase-rich domains (it is never present in garnet). Relict zoisite ($Zo_{86–88}$) is included in both garnet and clinopyroxene (Fig. 3a,d).

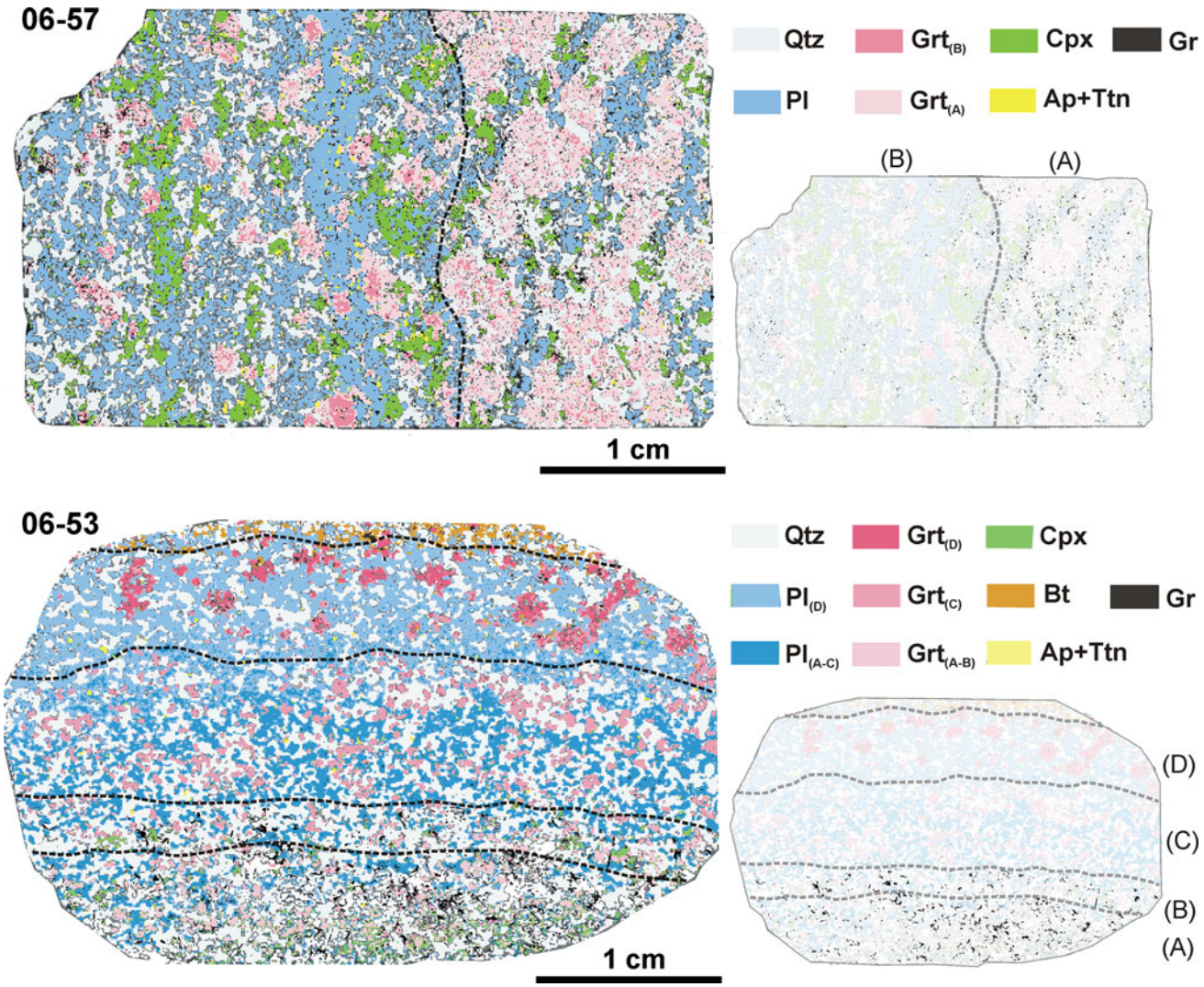

Fig. 2 Major elements μ-XRF maps of the whole thin sections of samples 06-53 and 06-57, with distinction of the different layers discussed in the text. Note the difference in graphite distribution within layers A and B

Layer B Plagioclase is the most abundant phase in this layer (40 vol%), followed by quartz (30 vol%), clinopyroxene (15 vol%), garnet (15 vol%) and minor zoisite. Graphite is far less abundant than in layer A and mainly occurs in the proximity to layer A. Plagioclase composition is the same as in layer A ($An_{95–96}$). Garnet occurs as: (1) large zoned porhpyroblasts (up to 500 μm in diameter) (Fig. 3e), with an almandine-rich core ($Alm_{29–32}Prp_{3–5}Grs_{55–57}Sps_{7–11}$) and a grossular-rich rim ($Alm_{20–25}Prp_{1–3}Grs_{71–73}Sps_{5–8}$) (Fig. 5b), this last locally showing a spongy appearance due to plagioclase ± quartz intergrowths (Fig. 3e); (2) small blebs and/or idioblasts associated with plagioclase ($Alm_{19–27}Prp_{1–3}Grs_{67–76}Sps_{4–7}$). Clinopyroxene forms large, weakly zoned crystals, locally intergrown with plagioclase (Fig. 3c), with a Mg- and Al-richer core and an Fe-richer rim ($X_{Mg} = 0.48–0.57$, Al = 0.04–0.06 a.p.f.u. vs. $X_{Mg} = 0.42–0.47$, Al = 0.02–0.04 a.p.f.u.). Relict zoisite ($Zo_{86–91}$) is mainly included in clinopyroxene (Fig. 3c).

Titanite is abundant as accessory mineral in both the layers and is included in all the phases.

Sample 06-53

Sample 06-53 is a fine-grained banded rock representative of the transition between the hosting anatectic paragneiss and the calc-silicate rock. Four different layers may be recognized, differing in grain size, mineral modes and mineral compositions; these layers are hereafter indicated as D to A moving from the hosting paragneiss towards the centre of the boudin (Fig. 2).

Layer D This layer is <1 cm in thickness, shows a granofelsic texture and is relatively coarse grained with

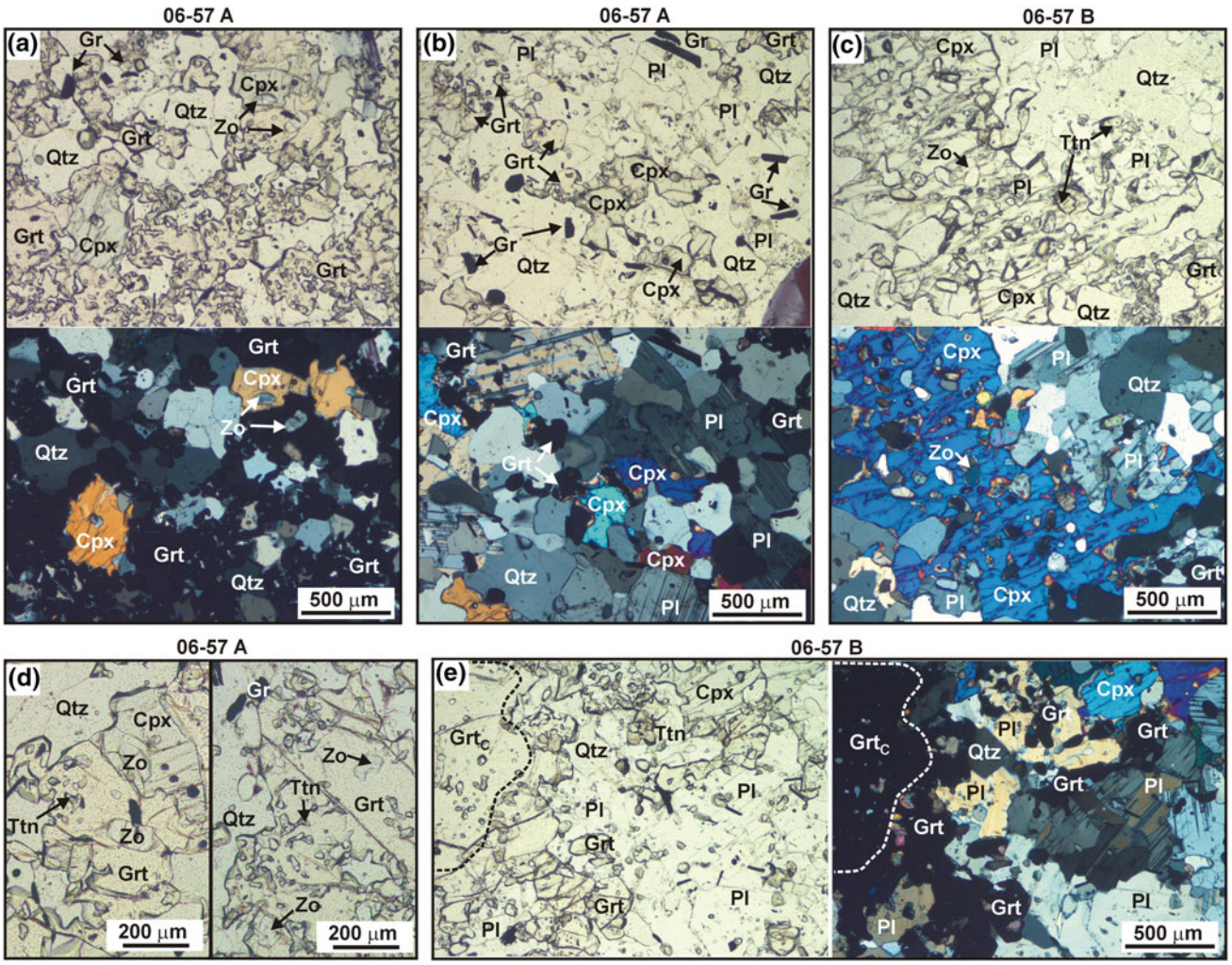

Fig. 3 Representative microstructures of sample 06-57. **a** Layer A: garnet porphyroblasts intergrown with quartz and partially replacing clinopyroxene. Note the zoisite inclusions in both garnet and clinopyroxene (*top right*). *Above*: Plane Polarized Light (PPL), *below*: Crossed Polarized Light (XPL). **b** Layer A: garnet intergrown with quartz, partially replacing clinopyroxene at its rim. *Above*: PPL, *below*: XPL. **c** Layer B: large clinopyroxene porphyroblast with inclusions of zoisite. *Above*: PPL, *below*: XPL. **d** Layer A: details showing the zoisite inclusions in garnet. **e** Layer B: Plurimillimetric garnet porphyroblast with a Grs-poor core (Grt_C) and a spongy Grs-rich rim (Grt_R): note the spongy appearance of the garnet rim due to the intergrowth with plagioclase and quartz. *Left*: PPL, *right*: XPL

respect to the other layers. It consists of plagioclase (56 vol%), quartz (30 vol%) and garnet (14 vol%). Garnet occurs as large porphyroblasts (up to 2 mm in size) with a spongy appearance due to numerous inclusions of quartz, plagioclase and minor biotite (Fig. 4a); its composition is homogeneous ($Alm_{67–68}Prp_{18–19}Grs_{8–9}Sps_6$) and dominated by the almandine component (Fig. 5a). Plagioclase is an andesine ($An_{35–41}$) (Fig. 5c).

Layer C This layer shows similar thickness and the same mineral assemblage than layer D, but the modal amounts of the minerals differ (plagioclase 45 vol%; quartz 41 vol%; garnet 14 vol%). Garnet forms mm-sized granoblasts with few inclusions of quartz and/or plagioclase (Fig. 4b). Its composition varies from $Alm_{62}Prp_{16}Grs_{12}Sps_9$ to $Alm_{57}Prp_{15}Grs_{19}Sps_{11}$ towards the transition to layer B (Fig. 5a). Plagioclase is coarse-grained and often crowded with small quartz inclusions; it is sharply zoned (Fig. 4b), with an andesine core ($An_{42–48}$) and a bytownite rim ($An_{80–83}$) (Fig. 5c).

Layer B This layer is characterized by the appearance of clinopyroxene and by an increase in the quartz modal amount (quartz 57 vol%; plagioclase 23 vol%; garnet 12 vol%; clinopyroxene 8 vol%). Coarse-grained graphite (up to 200 µm in length) appears in this layer, and increases in modal abundance towards the transition to level A (Fig. 2). Garnet is fine-grained (up to ~300 µm in size) and occurs as sub-idioblastic grains (Fig. 4c) locally overgrown by clinopyroxene. Its composition varies moving towards the

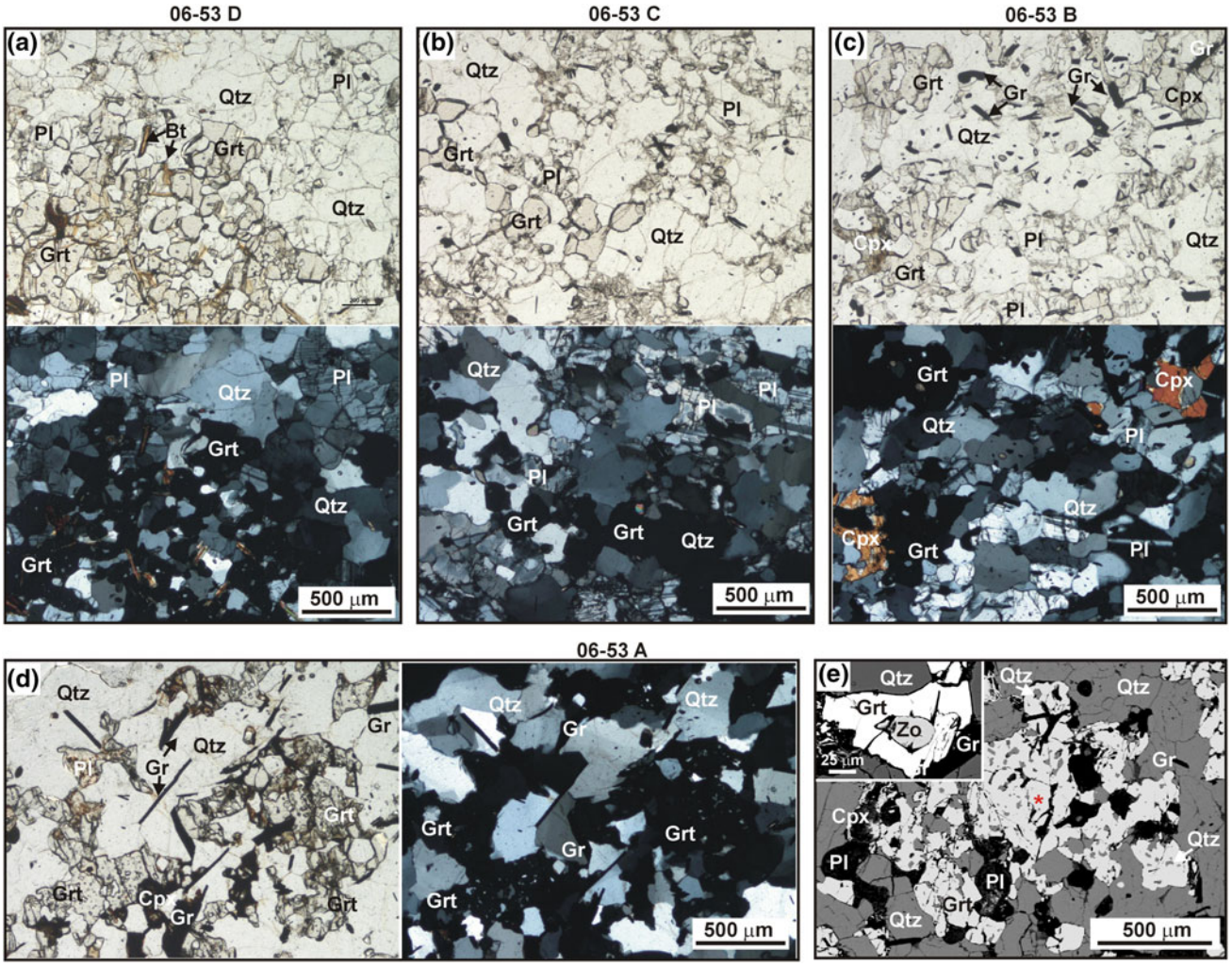

Fig. 4 Representative microstructures of sample 06-53. **a** Layer D: Garnet porphyroblast with inclusions of quartz, plagioclase and biotite. *Above*: PPL, *below*: XPL. **b** Layer C: note the strongly zoned plagioclase (*top right*). *Above*: PPL, *below*: XPL. **c** Layer B: note the coarse-grained clinopyroxene and the graphite flakes. *Above*: PPL, *below*: XPL. **d** Layer A: garnet is intergrown with fine-grained vermicular quartz. Note the coarse-grained graphite flakes. *Left*: PPL, *right*: XPL. **e** Layer A: BSE image showing the spongy appearance of garnet due to the intergrowth with vermicular quartz. The *red asterisk* indicates a very small calcite inclusion. Both plagioclase and clinopyroxene are pervasively replaced by fine-grained aggregates of hydrous minerals. The *inset* shows a zoisite relic included in garnet

transition to layer A, from $Alm_{42–33}Prp_{3–7}Grs_{37–42}Sps_{12–14}$ to $Alm_{22–27}Prp_{3–4}Grs_{60–65}Sps_{10–12}$ (Fig. 5a). Clinopyroxene occurs as subhedral mm-sized, weakly zoned, crystals, with an Mg-, Al-rich core ($X_{Mg} = 0.64–0.69$, Al = 0.06–0.07 a.p.f.u.) and a Fe-richer rim ($X_{Mg} = 0.48–0.59$, Al = 0.04–0.06). Plagioclase is anorthitic ($An_{92–96}$) (Fig. 5c) and partially replaced at its rim and along fractures by Al-rich phyllosilicates (probably clay minerals of the kaolinite group).

Layer A This layer is characterized by the sharp increase in both garnet and graphite modal amounts (quartz 43 vol%; garnet 35 vol%; plagioclase 13 vol%; clinopyroxene 8 vol%; graphite ca. 1 vol%) and by a reduction in the grain size. Graphite is abundant and forms large, randomly oriented, flakes located at the grain-boundaries of the main mineral phases (Fig. 4d). Garnet (up to ~500 μm in size) is mostly intergrown with fine-grained vermicular quartz, showing a typical spongy appearance (Fig. 4d, e). Small rounded grains of zoisite and rare calcite relicts are preserved within garnet (Fig. 4e). Garnet composition is relatively homogeneous ($Alm_{11–16}Prp_{1–2}Grs_{72–81}Sps_{5–9}$) and dominated by the grossular component (Fig. 5a). Both clinopyroxene and plagioclase are widely replaced by late clay minerals. Plagioclase is almost pure anorthite ($An_{95–96}$) (Fig. 5c) and is replaced by kaolinite, whereas clinopyroxene is rarely preserved and mostly replaced by a mixture of chlorite and smectite (Fig. 4d). Zoisite included in garnet is Zo_{87-91}.

Titanite is abundant as accessory mineral in layers A, B and C.

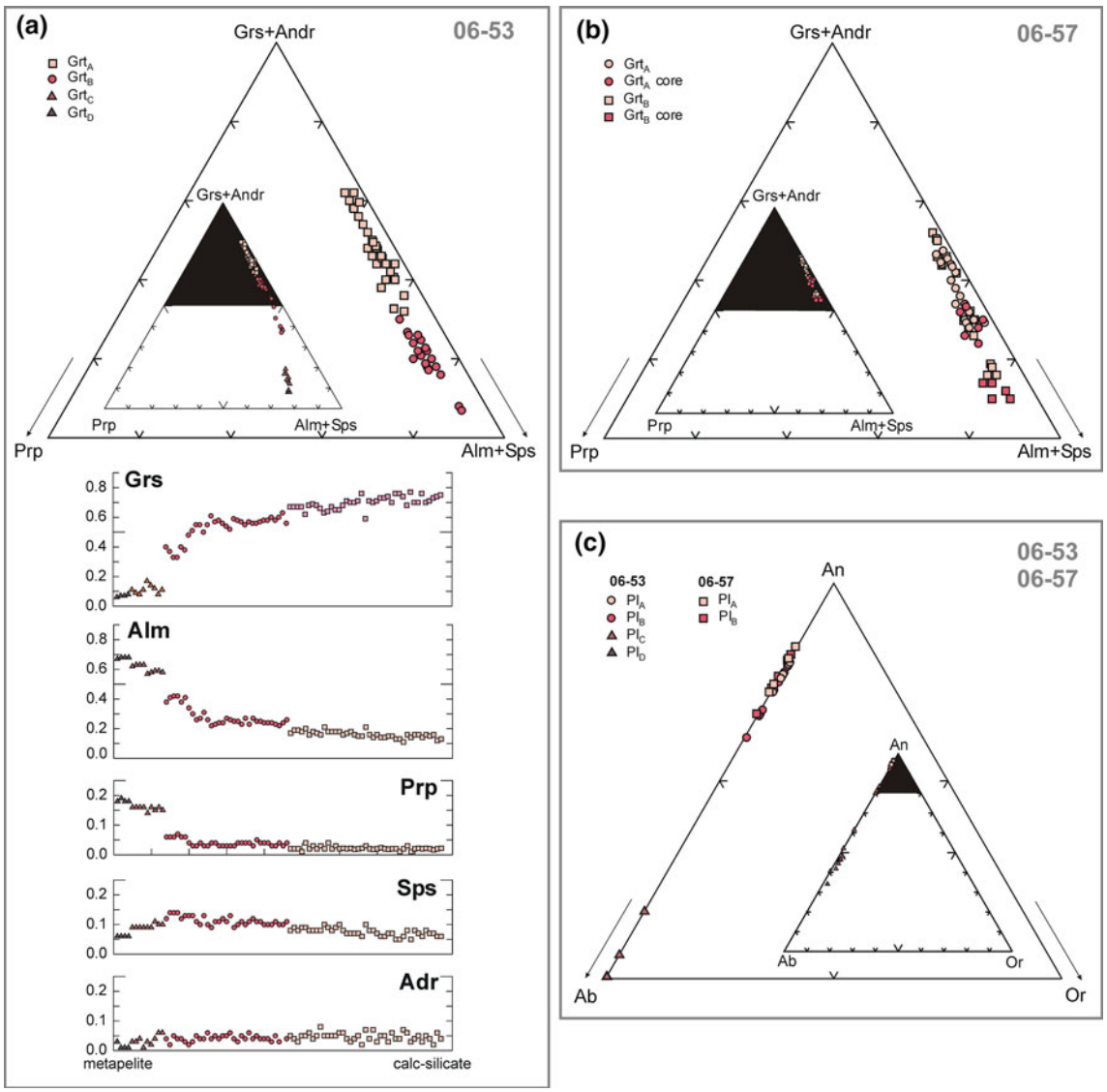

Fig. 5 **a**, **b** Garnet compositions plotted in the Prp–Grs+Andr–Alm + Sps diagram as a function of their position in the different layers (layers A to D for sample 06-53 and layers A to B for sample 06-57). For sample 06-53, the variation in garnet composition across an ideal traverse from the hosting metapelite towards the centre of the calc-silicate boudin is also reported. **c** Plagioclase compositions plotted in the Ab–An–Or diagram as a function of their position in the different layers (layers A to D for sample 06-53 and layers A to B for sample 06-57)

Bulk compositions

The bulk rock compositions of the different layers recognized in the studied samples 06-53 and 06-57 have been calculated by combining the mineral proportions obtained from the modal estimate of micro-XRF maps (Fig. 2) with mineral chemistry acquired at SEM–EDS. The bulk compositions are projected from quartz onto the plane ACF (Al_2O_3–CaO–FeO) (Fig. 6). This projection is particularly suitable to represent the grossular–almandine solid solution (joint Grs–Alm). Two other tie lines are relevant for our purposes, namely the Hed–Zo and Hed–An joint. Hedenbergite and zoisite are colinear with a Grs_{72} garnet, whereas hedenbergite and anorthite are colinear with a Grs_{66} garnet.

Layers 06-53D and 06-53C, representing the transition from the metapelite to the calc-silicate assemblage, are enriched in the Al_2O_3 component with respect to the other bulk compositions (Fig. 6). These two layers and the corresponding bulk compositions are not further considered in this paper. Layers 06-53A and 06-57A show similar bulk compositions and plot above the joint Hed–Zo, whereas layers 06-53B and 06-57B plot below the Hed–Zo joint but above the Hed–An joint. We will further discuss the

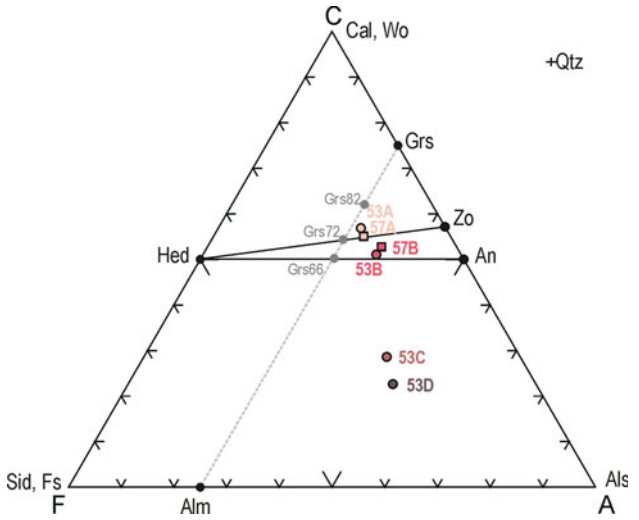

Fig. 6 Bulk compositions of the different layers in the studied samples 06-53 and 06-57 projected from quartz onto the ACF (Al_2O_3–CaO–FeO) diagram. The *dotted grey line* represents the solid solution Grs-Alm. The joints Hed–Zo and Hed–An are colinear with a Grs_{72} and a Grs_{66} garnet, respectively

consequences of these different bulk compositions for the development of different mineral assemblages and microstructures in the studied samples, highlighting the crucial role of the Hed–Zo joint.

Results

A petrogenetic grid for the system CFAS–H_2O–CO_2

The microstructural evidence described above demonstrates that clinopyroxene, zoisite, plagioclase, calcite and quartz are all involved in the garnet-forming reactions and that the garnet composition systematically varies as a function of its microstructural position. Robinson (1991), Sengupta and Raith (2002) and Dasgupta and Pal (2005) have considered the complexities that arise from the involvement of clinopyroxene in the garnet-forming reactions. In particular, Robinson (1991) and Sengupta and Raith (2002) demonstrated that in the system CFAS–CO_2 the reaction coefficients of one or more phases change continuously as a function of garnet composition, and that for certain compositions (i.e. singular compositions: Connolly and Trommsdorff 1991; Carmichael 1991; Robinson 1991; Abart et al. 1992), the sign of these coefficients may change. The consequence of these complexities is that at a specific *P*–*T* condition, garnet formation may occur at the expense of a particular mineral, while at another, it forms together with that mineral. In this paper, we extend the study of Sengupta and Raith (2002) to the mixed-volatile CFAS–CO_2–H_2O system, in order to evaluate the role played by zoisite in the garnet formation.

For mixed-volatile systems, fluid composition is a third variable to be considered in the modelling in addition to *P* and *T*. Mixed-volatile phase diagram projections, in which the volatile composition of the system is projected onto the *P*–*T* coordinate frame (e.g. Baker et al. 1991; Carmichael 1991; Connolly and Trommsdorff 1991; Omori et al. 1998; Castelli et al. 2007), are a means of simultaneously considering the effects of the three variables *P*, *T* and X^{fluid} on phase relations in the CFAS–H_2O–CO_2 system. To introduce these *P*–*T* projections, we first consider topologies in *P*–*T* phase diagrams at fixed fluid composition and in isobaric *T*–$X(CO_2)$ phase diagram sections.

P–*T* phase diagrams at constant fluid composition

In the H_2O–CO_2 fluid-saturated six-component system CaO–FeO–Al_2O_3–SiO_2–H_2O–CO_2 (CFAS–H_2O–CO_2), invariant points have 6 phases in addition to the omnipresent fluid. From each invariant point, as many as 6 non-degenerate univariant phase fields will emanate, each having 5 phases. The CFAS–H_2O–CO_2 system has been investigated at different $X(CO_2)$ values, in the 500–900 °C, 3–15 kbar *P*–*T* range (Fig. 7). For $X(CO_2) = 1$, the topology described by Sengupta and Raith (2002) is reproduced. The two invariant points [Wo, Zo] and [Grt, Zo] are stable towards the high-*T* side of the *P*–*T* range of interest, demonstrating that the petrogenetic grid discussed by Sengupta and Raith (2002) (their Fig. 9) is relevant at temperatures higher than those considered in this study. As discussed by Sengupta and Raith (2002), all the garnet-forming reactions have variable reaction coefficients that can be expressed in terms of garnet composition. The consequence is that garnet composition changes along each univariant curve as a function of *P* and *T*. For specific garnet compositions, the coefficients of one phase in the reaction is zero, a condition that defines a singular point on the univariant curve (e.g. Connolly and Trommsdorff 1991; Carmichael 1991; Robinson 1991; Abart et al. 1992). For $X(CO_2) < 0.6$, the [Me, Zo] invariant point is stabilized (Fig. 7), giving rise to the "alternate topology" discussed by Sengupta and Raith (2002).

As a consequence of the introduction of H_2O into the CFAS–CO_2 system, the degenerate univariant reaction Zo = Cal + An (reaction 5 in Fig. 7) is stabilized for $X(CO_2) < 1$. This reaction has a positive slope in the *P*–*T* space and occurs at progressively lower *P* with decreasing $X(CO_2)$, resulting in a progressive enlargement of the zoisite stability field at decreasing $X(CO_2)$ values. For $X(CO_2) < 0.2$, the conditions for the garnet-forming reactions (e.g. reaction 16 in Fig. 7) intersect those of reaction 5, such that two garnet-forming reactions are stabilized within the zoisite stability field in the *P*–*T* region

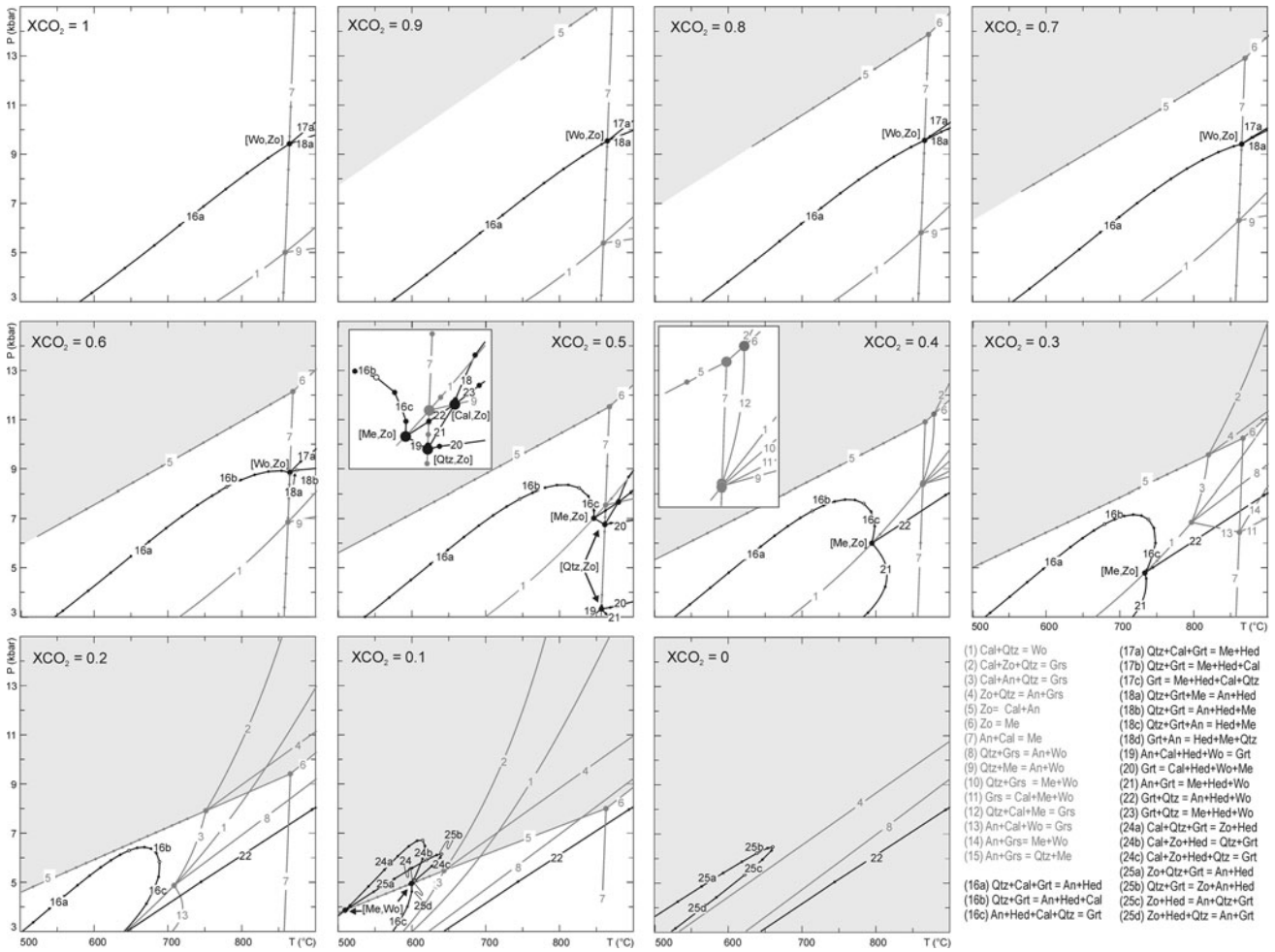

Fig. 7 *P–T* phase diagrams in the system CFAS–H_2O–CO_2 with excess fluid of constant composition ($X(CO_2)$ in the range 1–0). *Thick line*: univariant reactions; *solid large point*: invariant points; *empty point*: singular points. Equilibrium *curves* and *points* reported in *grey* refer to the degenerate reactions in the CAS–H_2O–CO_2 system. All reaction equations are written such that the high-*T* assemblage is on the *right side*. The *grey field* represents the zoisite stability field, limited by the degenerate CAS–H_2O–CO_2 reaction 5

of interest (reactions 24 and 25 in Fig. 7). These two garnet-forming reactions will be further discussed.

Influence of other components: MgO and Na_2O

The CFAS–H_2O–CO_2 system is simplified with respect to natural calc-silicate compositions. Components such as MgO, MnO, Na_2O and Fe_2O_3 may be potentially important in controlling the stability field of calc-silicate mineral assemblages. The influence of such components on the topology of the CFAS–CO_2 grid was discussed by Sengupta and Raith (2002). Since the studied samples do not show evidence for the presence of significant amounts of MnO and Fe_2O_3, we will limit our discussion to the influence of MgO and Na_2O.

MgO may enter in both clinopyroxene and garnet; however, garnet in the studied samples has low pyrope content ($Prp_{<5}$), suggesting that MgO is strongly partitioned into clinopyroxene. We have therefore approximated the introduction of MgO in the system by decreasing the hedenbergite activity in clinopyroxene (Fig. 8a). The reduction in *a*Hed strongly influences the position of the garnet-forming reactions in the *P–T* space, resulting in a significant expansion of the hedenbergite-bearing assemblages at the expense of the garnet-bearing ones.

Na_2O may enter in both plagioclase and scapolite and, at relatively high-*T*, is strongly partitioned in scapolite (see also Sengupta and Raith 2002). As a consequence, the introduction of Na_2O will result in a expansion of the scapolite-bearing assemblages at the expense of garnet-bearing assemblages. The effects of the introduction of Na_2O on the plagioclase stability field are approximated by decreasing anorthite activity and appear to be minor (Fig. 8b), at least for *X*An similar to those observed in the studied samples. Considering the average mineral

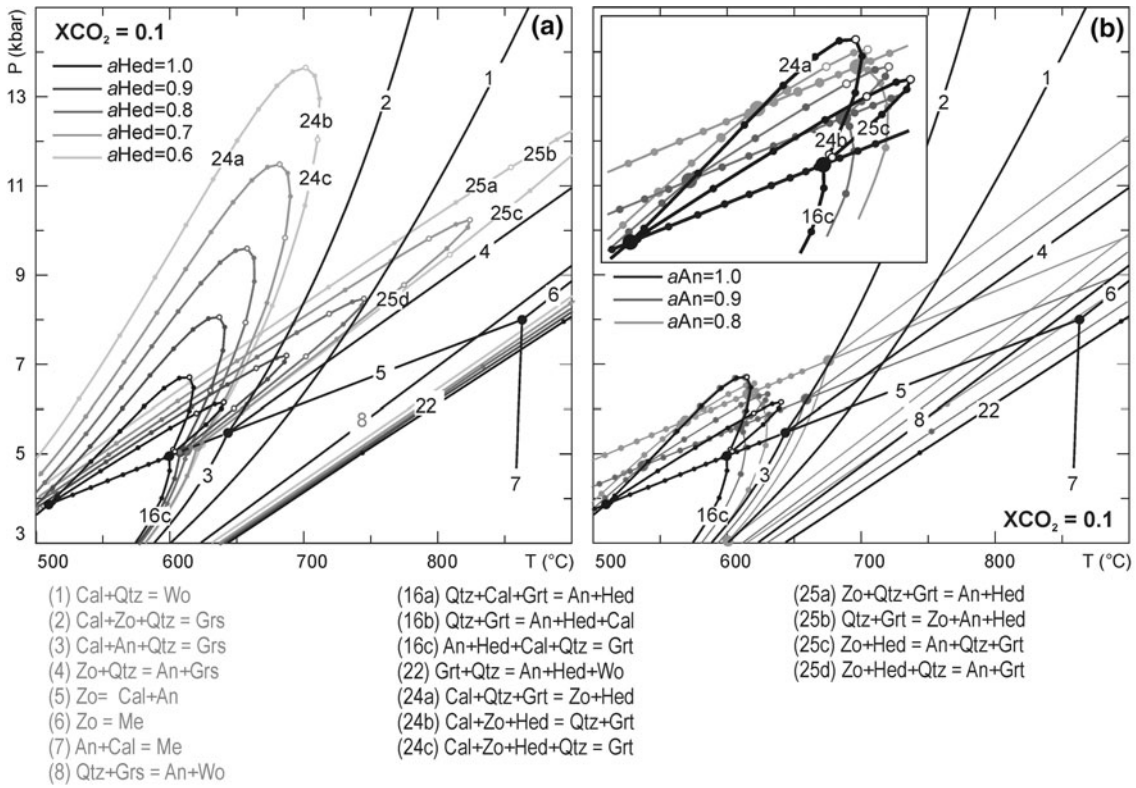

Fig. 8 *P–T* phase diagrams in the system CFAS–H_2O–CO_2 calculated at constant fluid composition of $X(CO_2) = 0.1$ and for different values of *a*Hed (**a**) and *a*An (**b**). The *curves* at *a*Hed = 1 and *a*An = 1 are the same as in the *P–T* phase diagram calculated at $X(CO_2) = 0.1$ in Fig. 7. Reaction labels as in Fig. 7. Equilibrium *curves* and *points* reported in *grey* refer to the degenerate reactions in the CAS–H_2O–CO_2 system

compositions in the studied samples, the following activities have been considered for the following calculations: *a*Hed = 0.6, *a*An = 1 and *a*Me = 0.8.

Garnet-forming reactions in the zoisite stability field

As mentioned before, two garnet-forming reactions occur in the zoisite stability field (i.e. reactions 24 and 25 in Fig. 7). Both the reactions have a parabolic shape and intersect reaction 5 at two invariants points, resulting from the duplication of the [Wo, Me] invariant point I_1 (Fig. 9). Reaction 24 (An, Me, Wo) involves the phases Cal, Qtz, Grt, Zo and Hed, whereas reaction 25 (Cal, Me, Wo) involves Qtz, Grt, Zo, Hed and An.

Reaction 24 (An, Me, Wo) has a singular point at Grs_{72}, at which the coefficients of calcite become zero. For $Grs_{<72}$, calcite is a product in the garnet-forming reaction (reaction 24a), whereas for $Grs_{>72}$, the calcite stoichiometric coefficient changes its sign (reaction 24b). A second singular point occurs for Grs_{82}, at which point the coefficient of quartz becomes zero. Quartz is a product in the garnet-forming reaction for $Grs_{<82}$ (reaction 24b), whereas it becomes a reactant for $Grs_{>82}$ (reaction 24c). Reaction 25 (Cal, Me, Wo) has three singular compositions (Fig. 9) at which the coefficients of zoisite (Grs_{66}), anorthite (Grs_{72}) and quartz (Grs_{82}) become zero, respectively. For $Grs_{<66}$, zoisite is a product in the garnet-forming reaction (reaction 25a), and it becomes a reactant for $Grs_{>66}$ (reaction 25b). For $Grs_{<72}$, anorthite is a reactant in the garnet-forming reaction (reaction 25b) and it becomes a product for $Grs_{>72}$ (reaction 25c). The behaviour of quartz is the same as in reaction 24. Beside the univariant equilibria 24 and 25, an additional garnet-bearing reaction curve emanates from the invariant points I_1: reaction 16 (Zo, Me, Wo) (Figs. 7, 9). Reaction 16 (Zo, Me, Wo) involves Qtz, Cal, Grt, An and Hed and has two singular points at Grs_{66} (the coefficient of Cal become zero) and Grs_{82} (the coefficient of Qtz becomes zero), respectively.

Singular points thus divide the Grt-bearing univariant reactions in three portions (reactions 24a, 24b and 24c), four portions (reactions 25a, 25b, 25c and 25d) and three portions (reactions 16a, 16b and 16c), respectively; grossular-richer garnet compositions are located along the higher-*T* portion of each univariant equilibria. The topological relationships between the Grt-bearing univariant equilibria and their conjugate singular curves (Abart et al. 1992) around the invariant point I_1 are reported in Fig. 10. The univariant equilibria 24 (An, Me, Wo) and 25 (Cal,

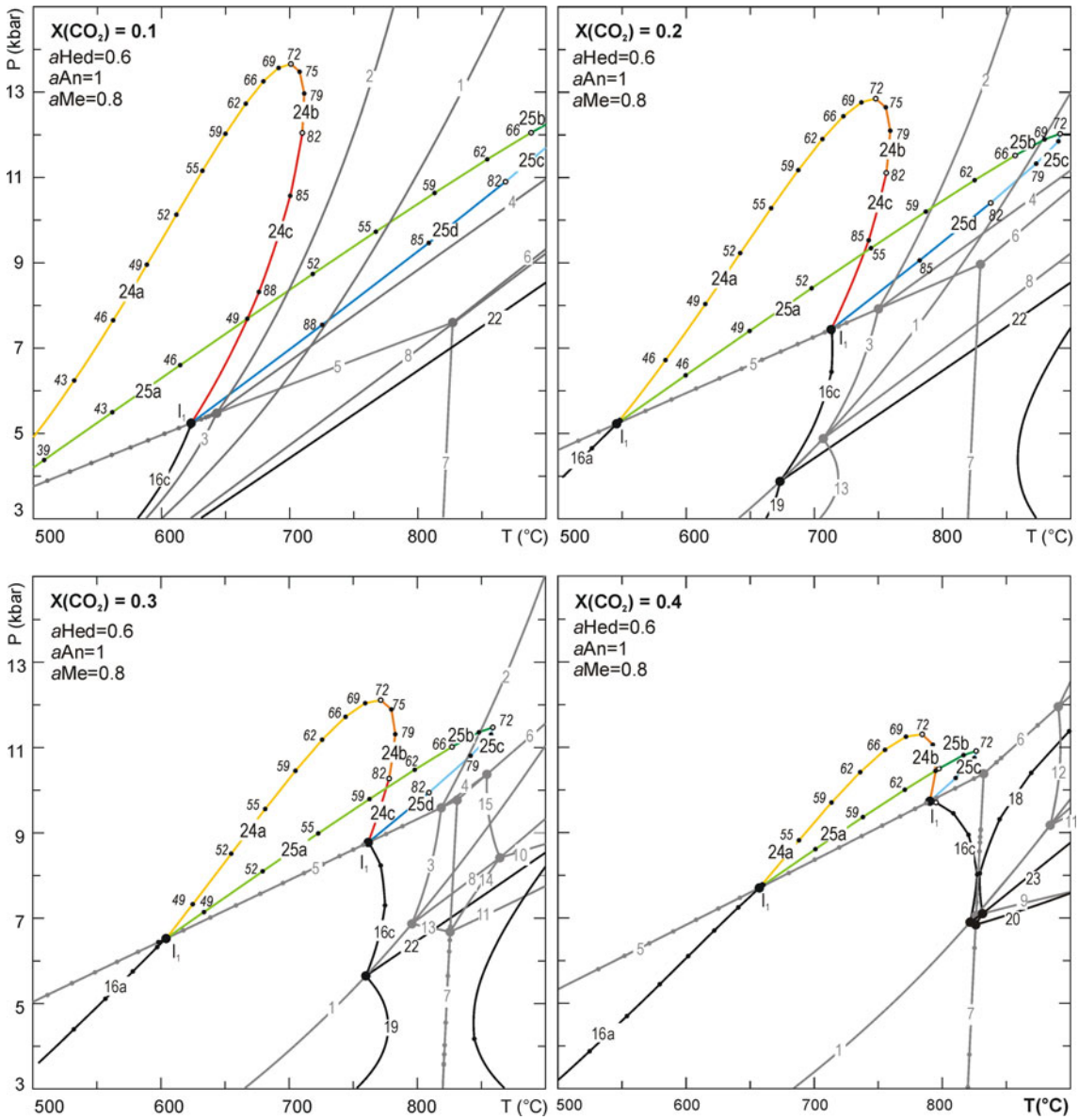

Fig. 9 *P–T* phase diagrams in the system CFAS–H_2O–CO_2 at constant fluid compositions ($X(CO_2)$ from 0.1 to 0.4) calculated for *a*Hed = 0.6 and *a*Me = 0.8. *Thick line*: univariant reactions; *solid large point*: invariant points; *empty point*: singular points and singular compositions (% Grs); *solid small points* indicate the variation in garnet composition along the univariant *curves* (% Grs, in italic). Equilibrium *curves* and *points* reported in *grey* refer to the degenerate reactions in the CAS–H_2O–CO_2 system. Reaction labels as in Fig. 7

Me, Wo) are connected by a common singular curve [S_{72}(An, Cal, Me, Wo) in Fig. 10], which is tangent to the Grs_{72} singular points. Similarly, the univariant equilibria 16 (Zo, Me, Wo) and 25 (Cal, Me, Wo) are connected by a common singular curve [S_{66}(Zo, Cal, Me, Wo) in Fig. 10], tangent to the Grs_{66} singular points. Furthermore, as a consequence of the compositional degeneracy among Zo, An and Cal, an additional invariant point (I_2 in Fig. 10) is stabilized on the Grt-absent degenerate univariant reaction 5. This invariant point I_2 is defined by the intersection of reaction 5 with the three singular curves S_{82}(An, Qtz, Me, Wo), S_{82}(Cal, Qtz, Me, Wo) and S_{82}(Zo, Qtz, Me, Wo), which are tangent to the univariant equilibria 24 (An, Me, Wo), 25 (Cal, Me, Wo) and 16 (Zo, Me, Wo), respectively, at the Grs_{82} singular points. A peculiarity of this system is that the Grt-absent reaction 5 occurs in the presence of garnet at invariant point I_2 (see Abart et al. 1992 for further explanations).

Sensitivity of different bulk compositions to garnet-forming reactions

Chemographies provide an alternative view of the garnet-forming reactions 24 and 25 as a function of *T* and

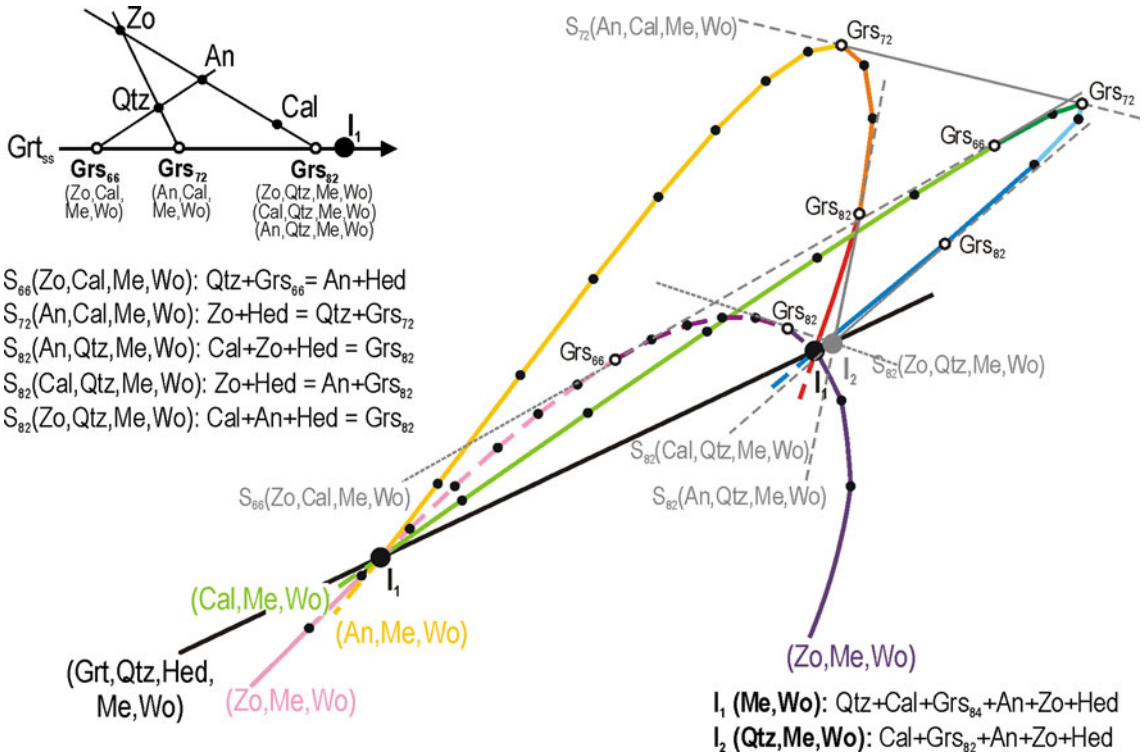

Fig. 10 Topological relations between the garnet-bearing univariant equilibria and their conjugate singular *curves* around the invariant point I_1. The key reactions are the garnet-absent degenerate reaction (5) and the three garnet-bearing CFAS–H_2O–CO_2 reactions 16 (Zo, Me, Wo), 24 (An, Me, Wo) and 25 (Cal, Me, Wo). *Thick line*: univariant reactions (*continuous*: stable; *dashed*: metastable); *solid large point*: invariant points; *empty point*: singular points and singular compositions; *grey thin lines*: singular (*ccurves ontinuous*: stable; *dashed*: metastable; *dotted*: doubly metastable); *grey point*: additional invariant point defined by the intersection of singular *curves* and reaction 5. The *top-left* sketch summarizes the chemographic relations among the phases involved (Qtz, Zo, An and Cal) and the garnet binary solid solution. Grs_{66}, Grs_{72} and Grs_{82} represent singular solution compositions labelled by the phases absent from the correspondent singular equilibria

P (Fig. 11) and are useful for understanding the influence of bulk composition. Reaction 24a (Cal + Qtz + Grt = Zo + Hed) is marked by the disappearance of the join Cal–Grt ($Grs_{<66}$) and the appearance of the joint Hed–Zo. The bulk compositions of both layers A (06-53A, 06-57A) and B (06-53B, 06-57B) are affected by this reaction, but with different final assemblages. In fact, either garnet ($Grs_{<66}$) or calcite are virtually completely consumed through reaction 24a for bulk compositions A versus B, respectively. Reaction 24b (Cal + Zo + Hed = Grt + Qtz) occurs when the assemblage Cal + Hed + Zo gives place to the joint Grt–Qtz ($Grs_{>72}$). Only the bulk composition A, located above the joint Hed–Zo, is affected by this reaction. Because the calculated chemographies (Fig. 11) assume quartz in excess, the topological representation of reaction 24c (Cal + Zo + Hed + Qtz = Grt) is the same as that of reaction 24b, but in this case, the assemblage Cal + Hed + Zo + Qtz gives place to Grt ($Grs_{>82}$). Reaction 24c is only "seen" by bulk composition A.

Reaction 25a (Zo + Qtz + Grt = An + Hed) is marked by the disappearance of the joint Grt–Zo ($Grs_{<66}$) and the appearance of the joint Hed–An (Fig. 11). This reaction is only affected by bulk composition B. Reaction 25c (Zo + Hed = An + Qtz + Grt) and 25d (Zo + Hed + Qtz = An + Grt) are marked by the disappearance of the joint Hed–Zo, which is replaced by the joint Grt–An ($Grs_{>72}$), and they are affected by both compositions A and B.

The computed phase relations show that, at the same *P*–*T* conditions, the final assemblages and microstructures of calc-silicate rocks are controlled by their initial bulk compositions. In this regard, the joint Hed–Zo plays a crucial role: bulk compositions A plotting above the joint Hed–Zo are sensitive to the whole reaction 24 (24a, 24b, 24c) and to the high-*T* portion of reaction 25 (25c, 25d), whereas bulk compositions B plotting below the joint Hed–Zo are sensitive to the low-*T* portion of reaction 24 (24a) and the whole reaction 25 (25a, 25b, 25c, 25d). The main consequence for the studied samples is that garnet in layers A and B grew through different garnet-forming reactions, resulting in different microstructures and compositions. This aspect will be discussed in the next sections.

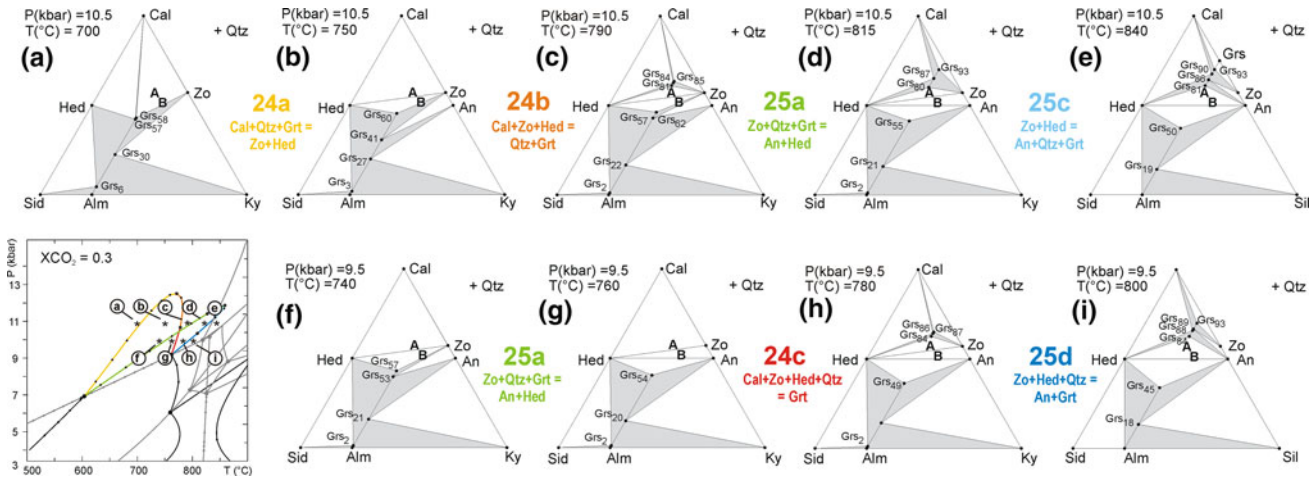

Fig. 11 Isobaric-isothermal chemographies in the system CFAS–H_2O–CO_2 (excess fluid of constant composition) showing the sensitivity of bulk compositions A and B to the garnet-forming reactions 24 (An, Me, Wo) and 25 (Cal, Me, Wo). The equilibrium garnet compositions are reported along the Alm–Grs joint

Isobaric T–$X(CO_2)$ sections

T–$X(CO_2)$ sections at fixed pressure are the most conventional diagrams used to interpret H_2O–CO_2 mixed-volatile equilibria in calc-silicate rocks (e.g. Kerrick 1974), being particular useful to constrain fluid composition during metamorphism (provided that the P–T evolution of the samples is independently known).

The computed topology of most of the degenerate univariant CASV reactions (Fig. 12) is in agreement with the results of Gordon and Greenwood (1971). Equilibrium 5 constrains the zoisite stability field on its low $X(CO_2)$ side (see also Kerrick 1974). The particular slope and curvature of the two garnet-forming reactions 24 and 25 derive from the fact that, at specific singular points, H_2O and/or CO_2 change their side, so that each univariant reaction is divided into different types of mixed-volatile equilibria. According to the classification of Kerrick (1974), reaction 24a is a "type 5" equilibrium (i.e. H_2O and CO_2 are on opposite side) and has therefore an S shape in the T–$X(CO_2)$ space; reactions 24b and 24c are "type 4" equilibria (i.e. H_2O and CO_2 are on the same side) and are concave downward with a maximum at a $X(CO_2)$ value defined by the stoichiometry of the reactions. Reaction 25 only involves H_2O ("type 3" equilibrium of Kerrick 1974) and should be therefore concave downward and asymptotic towards $X(CO_2) = 1$. The particular shape of the whole reaction 25 in the T–$X(CO_2)$ space is due to the fact that at the Grs_{66} singular point, the reaction coefficient of H_2O changes sign so that equilibrium 25b is a hydration reaction (i.e. concave upward and asymptotic towards $X(CO_2) = 1$) rather than a dehydration reaction, as equilibria 25a, 25c and 25d.

Mixed-volatile phase diagram projection

The theoretical basis and the relations between the mixed-volatile P–T projections and the commonly used T–$X(CO_2)$ sections are discussed in Connolly and Trommsdorff (1991). For our purposes, it is useful to remember that: (1) fluid-present univariant curves in a mixed-volatile P–T projection correspond to invariant points in the correspondent isobaric T–$X(CO_2)$ sections, and (2) in a mixed-volatile P–T projection, the composition of the fluid continuously changes along the univariant curves (see Connolly and Trommsdorff 1991 for further details).

In the P–T projection calculated for the system CFAS–H_2O–CO_2 (using the same aHed and aMe used in the previous calculations), both fluid and garnet may change their compositions along univariant curves. As a consequence, different types of equilibria may be recognized (Fig. 13a):

1. fluid-absent degenerate CAS univariant curves (e.g. equilibria 7 and 8, dotted grey curves) and CFAS univariant curves (e.g. equilibrium 22, dotted black curves);
2. degenerate CAS–H_2O–CO_2 univariant curves with fluid of constant composition (e.g. equilibria 1, 2, 4 and 9, dashed grey curves).
3. degenerate, CAS–H_2O–CO_2 univariant curves with fluid of variable composition (e.g. equilibria 27, 28 and 29, thin continuous grey curves).
4. CFAS–H_2O–CO_2 univariant curves with fluid of constant composition and garnet of variable composition (e.g. equilibria 16, 17, 18, 24 and 25): these equilibria are the same as those already discussed for the P–T sections at constant fluid composition.

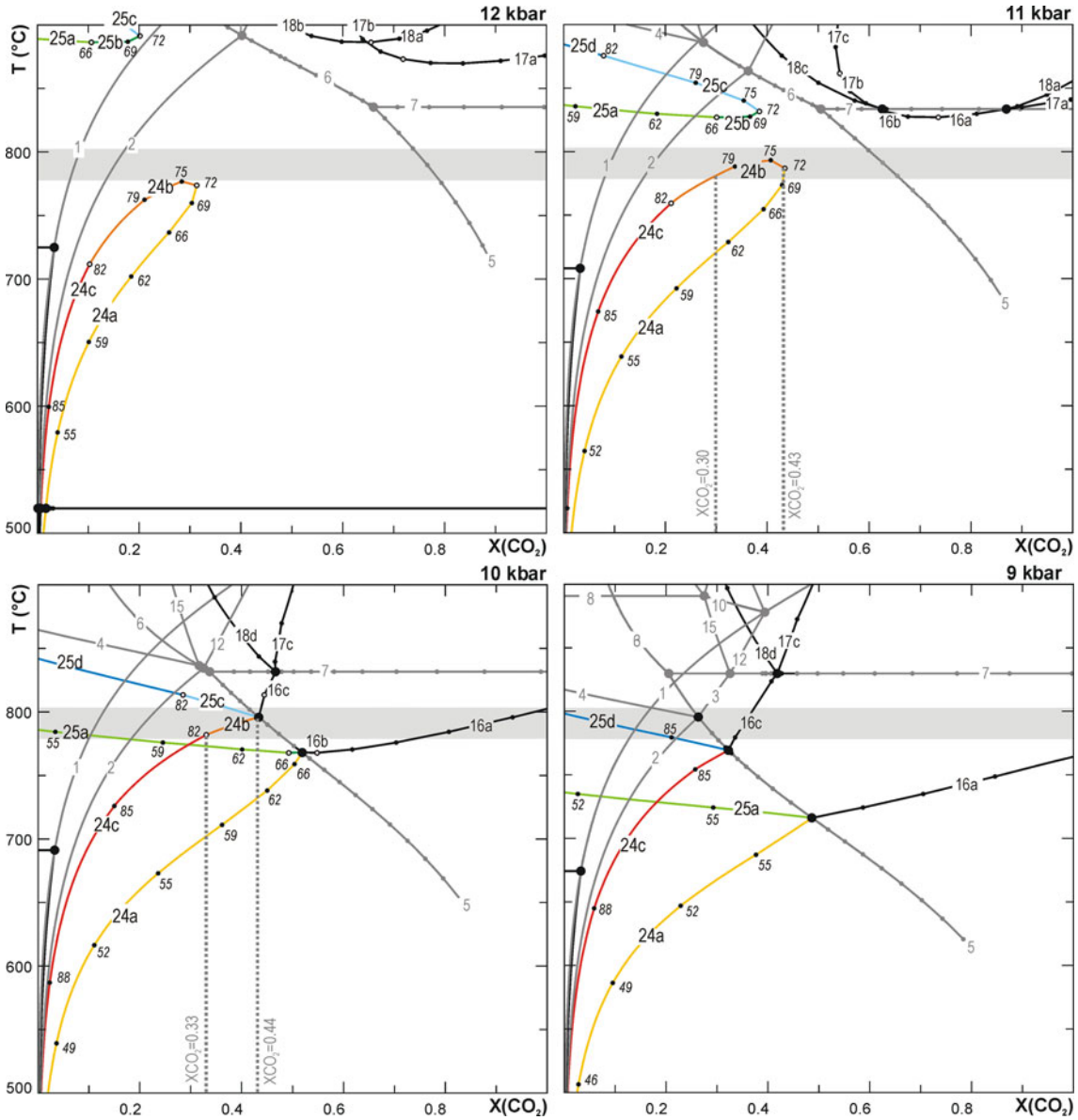

Fig. 12 Isobaric T–$X(CO_2)$ phase diagrams sections in the system CFAS–H_2O–CO_2 at pressures from 12 to 9 kbar, calculated for aHed = 0.6 and aMe = 0.8. *Thick line*: univariant reactions; *solid large point*: invariant points; *empty point*: singular points and singular compositions (% Grs); *solid small points* indicate the variation in garnet composition along the univariant *curves* (% Grs, in italic). Equilibrium *curves* and *points* reported in *grey* refer to the degenerate reactions in the CAS–H_2O–CO_2 system. Reaction labels as in Fig. 7. The *shaded area* corresponds to peak-T conditions as inferred from the hosting anatectic paragneiss (see Groppo et al. 2009). The *grey dotted lines* constrain the composition of the fluid in equilibrium with garnet and quartz growing through reaction 24b (see text for discussion)

5. CFAS–H_2O–CO_2 univariant curve with both fluid and garnet of variable composition (equilibrium 26). Three singular points occur along this curve at which the reaction coefficients of calcite, zoisite and fluid (Grs_{66}), anorthite (F_{48}, corresponding to $X(CO_2) = 0.48$) and quartz (Grs_{82}) become zero (Fig. 13b). These singular points divide reaction 26 in four portions: (26a) Cal + Zo + Grt + Qtz = An + Hed + F, (26b) Grt + Qtz + F = Cal + Zo + An + Hed, (26c) Cal + Zo + Hed = Grt + An + Qtz + F, (26d) Cal + Zo + Hed + Qtz = Grt + An + F (Fig. 13a). Garnet composition ranges from $Grs_{<42}$ to $Grs_{>92}$, with grossular-richer garnet compositions located along the higher-T portion of equilibrium 26. Fluid composition varies between F_8 and F_{51} ($0.08 < X(CO_2) < 0.51$), with the highest $X(CO_2)$ values towards the higher-P portion of equilibrium 26 (Fig. 13b). Due to the particular direction of fluid composition variation along the univariant equilibrium 26, two additional singular points with an extreme fluid composition (i.e. F_0) occur

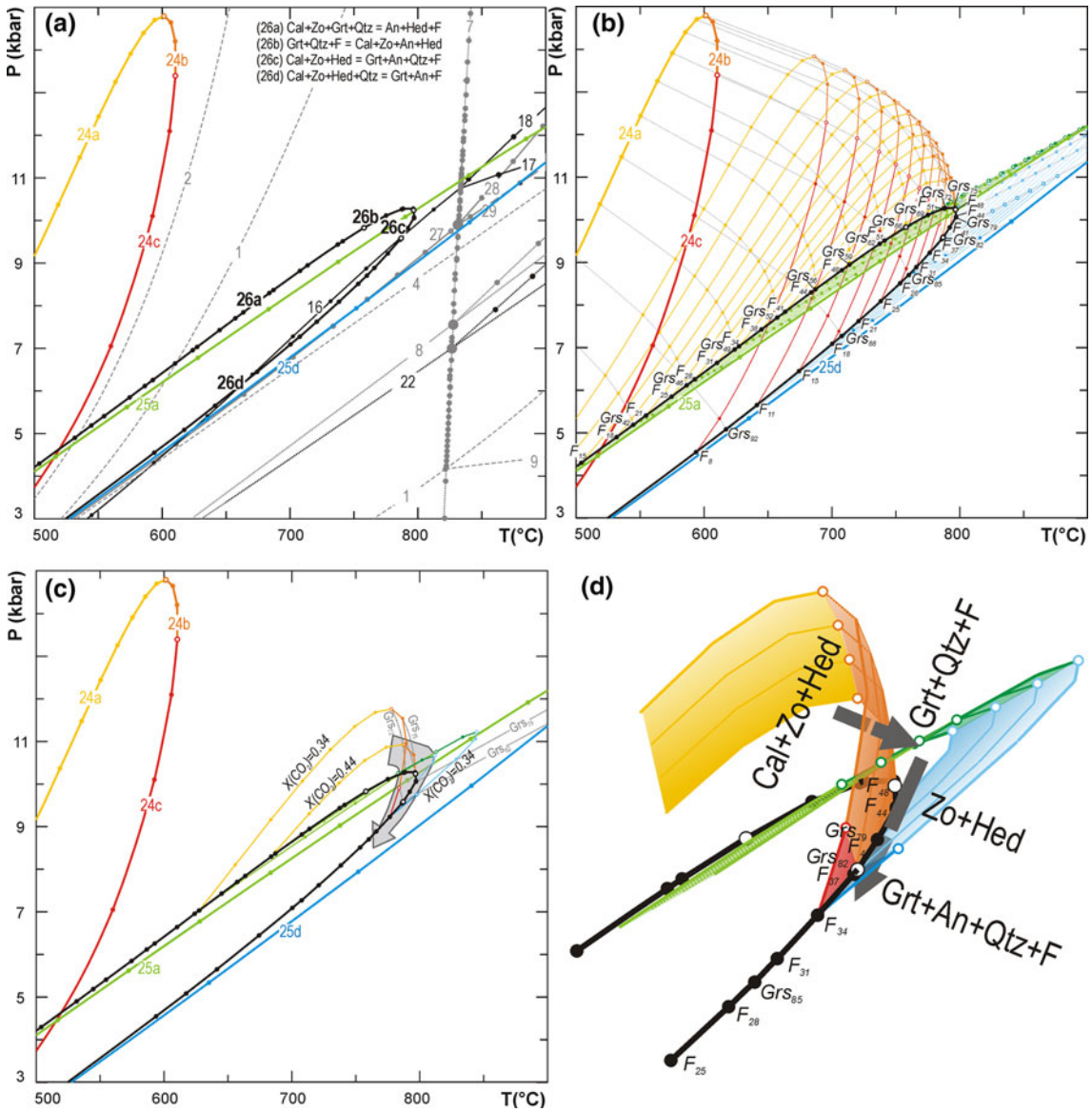

Fig. 13 Mixed-volatile *P–T* projection in the system CFAS–H_2O–CO_2 calculated for *a*Hed = 0.6 and *a*Me = 0.8. **a** *Dotted grey* and *black lines*: fluid-absent univariant reactions (*grey*: degenerate CAS–H_2O–CO_2 *curves*); *dashed grey lines*: fluid-present degenerate CAS–H_2O–CO_2 univariant reactions with fluid of extreme composition (pure H_2O or pure CO_2); *continuous grey lines*: fluid-present degenerate CAS–H_2O–CO_2 univariant reactions with fluid of variable composition; *continuous thin black* and *coloured lines*: fluid-present CFAS–H_2O–CO_2 univariant reactions with garnet of variable composition; *continuous thick black line*: fluid-present CFAS–H_2O–CO_2 univariant reaction with both fluid and garnet of variable composition. *Solid large points*: invariant points; *empty point*: singular points. Reaction labels as in Fig. 7. **b** Detail of the reaction 26 (the fluid and garnet composition is reported at each *small point*). Among the other univariant *curves*, only equilibria 24 and 25 are reported, with the correspondent fluid isopleths (*thin lines*). **c** Selected equilibria from **a** and **b**, relevant for constraining the *P–T–X*^{fluid} evolution in the studied samples (see discussion in the text). The *P–T* evolution inferred from the hosting anatectic paragneiss is reported with a *grey arrow*. **d** 3D representation of the selected equilibria reported in **c**

along the equilibria 26a and 26d at *P–T* conditions outside the considered *P–T* range. The univariant equilibria 25a and 25d represent the singular curves conjugate to these extreme singular points. Similarly, equilibrium 27 is the singular curve conjugate to the Grs_{100} singular point located on equilibrium 26d at *P–T* conditions outside the *P–T* range of interest.

In the *P–T–X* space, the univariant reaction curves 24 and 25 become reaction surfaces, which can be thought of as the envelope of all stable fluid isopleths (Fig. 13d). The intersection of these reaction surfaces defines the univariant reaction 26 (which corresponds to the duplicated invariant point I_1 in the isobaric *T–X*(CO_2) sections of Fig. 12).

Table 1 Predicted versus observed mineral assemblages and compositions

Eq.	Reactants	Products	Predicted microstructures	Observed microstructures			
				06-57A	06-53A	06-57B	06-53B
24a	Cal + Qtz + Grt	Zo + Hed	Early Grt ($Grs_{<72}$) replaced by Cpx			X	X
24b	Zo + Hed + Cal	Qtz + Grt	Grt ($Grs_{72–83}$) intergrown with Qtz	X	X		
			Grt ($Grs_{72–83}$) replacing Cpx	X	Ambiguous		
			Zo relics in Grt ($Grs_{72–82}$)	X	X		
			Cal relics in Grt ($Grs_{72–82}$)		X		
24c	Zo + Hed + Cal + Qtz	Grt	Grt ($Grs_{>82}$) replacing Cpx/Zo				
25a	Zo + Qtz + Grt	An + Hed	early Grt ($Grs_{<66}$) replaced by Cpx			Ambiguous	X
			An + Hed symplectites replacing early Grt ($Grs_{<66}$)			X	
			Zo relics in Cpx/An			X	
25b	Qtz + Grt	An + Hed + Zo	Early Grt ($Grs_{66–72}$) replaced by Cpx				
25c	Zo + Hed	Qtz + Grt + An	Grt ($Grs_{72–82}$) intergrown/associated with An + Qtz	X		X	
25d	Zo + Hed + Qtz	Grt + An	Grt ($Grs_{>82}$) intergrown/associated with An				

Discussion

P–T–X^{fluid} evolution

Microstructures and mineral compositions in the studied samples may be interpreted in the light of the newly calculated phase relations in the CFAS–H_2O–CO_2 system. Table 1 summarizes and compares the garnet-bearing microstructures resulting from reactions 24 and 25, as predicted by the P–T, T–X and P–T–X diagrams of Figs. 9, 12 and 13 and those observed in the studied calc-silicate rocks.

Most of the garnets from levels A (in both samples 06-57 and 06-53) have a spongy appearance due to quartz intergrowths, include abundant zoisite and minor calcite relicts and partially replace clinopyroxene at the rim (Figs. 3, 4). These garnets are rich in the grossular component ($Grs_{67–81}$) (Fig. 5). The high grossular content is consistent with garnet growth through reaction 24b (Cal + Zo + Hed = Grt + Qtz) along an heating P–T path because reaction 24b is mostly T-dependent (Fig. 9). The large garnet porphyroblasts in sample 06-57A do not preserve any almandine-rich relict core, suggesting that prograde Grs-poor garnet should have been completely consumed through reaction 24a (see Fig. 11, chemographies a and b).

Garnets from levels B (06-57B and 06-53B) show a wider compositional range than garnet from layers A, depending on microstructural position. Relatively Fe-rich garnets ($Grs_{55–57}$) are included in clinopyroxene porphyroblasts and are preserved as relict cores within large porphyroblasts (Figs. 3d, e, 5), suggesting that reaction 24a (Cal + Qtz + Grt = Zo + Hed) was likely active during the prograde evolution but that it did not result in the complete consumption of early garnet, in agreement with the chemographic phase relations (Fig. 11). On the contrary, the porphyroblasts rims are intergrown with plagioclase and quartz (Fig. 3e) and are richer in grossular ($Grs_{67–76}$) (Fig. 5): this microstructure is consistent with garnet growth through reactions 25c along either an heating or decompression P–T path, because reaction 25 has a moderate positive slope in the P–T space (Fig. 9). The same reaction may also explain the occurrence of the small Grs-rich garnet idioblasts associated with plagioclase, which are also abundant in layers B.

The P–T evolution of the studied calc-silicate rocks is derived from that of the hosting Grt + Kfs + Bt + Ky ± Sil anatectic gneisses (Groppo et al. 2009; sample 06-38). Petrological modelling of the hosting gneisses suggests a prograde heating path associated with minor decompression up to peak P–T conditions of 780–800 °C, 10.5–11.0 kbar, followed by cooling and decompression at ca. 750 °C, 8.5–9.0 kbar (Fig. 13c). This independently known P–T path combined with the observed microstructures may be used to constrain fluid composition during the metamorphic evolution of the studied calc-silicate rocks. A first constraint is given by the growth of garnet in layers A through reaction 24b. The T–$X(CO_2)$ sections at 10–11 kbar (Fig. 12) show that this reaction: (1) occurs at $770 < T < 800$ °C and is therefore consistent with the peak P–T estimates, and (2) constrains the fluid composition at $0.20 < X(CO_2) < 0.44$ (i.e. F_{20}–F_{44}). This constraint is consistent with the mixed-volatile P–T projection of Fig. 13c, d. According to the topological relations of

Table 2 Fluid/rock ratios calculated for reaction 24b

790 °C, 11 kbar	V mol (cm^3/mol)	Stoich. coeff.	Maximum Grt vol%		06-53		06-57	
			no moles	V (cm^3)	no moles	V (cm^3)	no moles	V (cm^3)
Reactants			*Consumed*		*Consumed*		*Consumed*	
Cal	37.23	0.48	0.19	7.05	0.13	4.94	0.16	5.78
Zo	138.41	0.67	0.26	36.60	0.19	25.62	0.22	30.01
Hed	69.02	0.59	0.23	16.07	0.16	11.25	0.19	13.18
Products			*Produced*		*Produced*		*Produced*	
Qtz	23.09	0.18	0.07	1.64	0.05	1.15	0.06	1.35
Grs_{80}	126.68	1.00	0.39	50.00	0.28	35.00	0.32	41.00
H_2O	19.37	0.33	0.13	2.52	0.09	1.77	0.11	2.07
CO_2	34.97	0.48	0.19	6.63	0.13	4.64	0.16	5.43
Gr	5.298		0.19	1.00	0.13	0.70	0.16	0.82
			V rock (cm^3)	100.00		100.00		100.00

		V fluid (cm^3)	Fluid/rock ratios	V fluid (cm^3)	Fluid/rock ratios	V fluid (cm^3)	Fluid/rock ratios
Equilibrium fluid: $X(CO_2)_2$	0.36	9.15	0.091	6.40	0.064	7.50	0.075
Infiltrating fluid (1): $X(CO_2)_2$	0.00	4.00	0.131	2.80	0.092	3.28	0.108
Infiltrating fluid (2): $X(CO_2)_2$	0.50	5.61	0.148	3.93	0.103	4.60	0.121

Figs. 9 and 13c, reaction 25c may have been active during either prograde heating or during early decompression at about 780-800 °C, 10 kbar. This constrains fluid composition at $0.30 < X(CO_2) < 0.44$ (Figs. 12, 13c, d).

According to microstructural and mineral chemical data and to the modelled P–T–X grids, the P–T–X_{fluid} evolution of the studied calc-silicate rocks may be therefore summarized as follows (Fig. 13d):

- prograde heating up to peak-T of ca. 800 °C (at about 10–11 kbar) involved the growth of Grs-rich garnet ($Grs_{67–81}$) in equilibrium with quartz at the expenses of zoisite, clinopyroxene and calcite, through reaction 24b. This reaction released a CO_2-rich fluid (F_{20}–F_{44}) and led to the total consumption of the earlier Grs-poor prograde garnet ($Grs_{55–57}$) in layers A. Early Grs-poor garnet is instead partially preserved in layers B;
- a Grs-rich garnet ($Grs_{67–76}$) grew in equilibrium with plagioclase and quartz during either prograde heating or early decompression through reaction 25c. This reaction released a CO_2-rich fluid with approximately the same composition as that released through reaction 24b (F_{30}–F_{44}).

Fluid–rock interactions and the origin of graphite

Closed- versus open-system behaviour

Thermodynamic modelling demonstrates that calc-silicate rocks of appropriate composition may act as CO_2-source during prograde heating and/or early decompression, because CO_2-rich fluids are released through garnet-forming reactions in the zoisite stability field. The amount and composition of the fluid released during garnet growth change as a function of garnet composition, the $X(CO_2)$ increasing with the increase in the grossular component of garnet (see Fig. 13). The widespread coexistence of both reactants and products of the garnet-forming reactions in the studied samples suggests internal buffering of pore fluid by mineral–fluid equilibria. In order to confirm this hypothesis, the ambient fluid/rock ratios in layers A of the studied calc-silicate rocks have been calculated following the method of Ferry (1983) and considering the stoichiometrically balanced reaction 24b:

$$0.48\,\mathrm{Cal} + 0.67\,\mathrm{Zo} + 0.59\,\mathrm{Hed} = 0.18\,\mathrm{Qtz} + 1.00\,\mathrm{Grs_{80}} + 0.33\,\mathrm{H_2O} + 0.48\,\mathrm{CO_2}$$

The following input parameters have been used: $T = 790$ °C, $P = 11$ kbar, molar volumes of garnet (Grs_{80}), CO_2 and H_2O from Holland and Powell (1998), modal % of garnet = 50 vol%. The equilibrium fluid composition $X(CO_2) = 0.36$ has been calculated from the isobaric T–$X(CO_2)$ grid for the correspondent univariant assemblage; the composition of the infiltrating fluid has been set to $X(CO_2) = 0$ (i.e. pure H_2O), and $X(CO_2) = 0.5$. Since the observed garnet modal volumes are lower than the input value in both the samples, the calculated fluid/rock ratio represents a maximum estimate. The results of the calculation are reported in Table 2. Maximum garnet production (50 vol%) is possible with a fluid/rock ratio of

0.091 in the case of no fluid infiltration, 0.131 in the case of hydrous fluid flux and 0.148 for infiltration of intermediate fluid. These low fluid/rock ratios exclude the possibility of a pervasive external fluid flushing in the studied samples; if a significant amount of external fluid were fluxed in (i.e. fluid/rock ratio >1), in fact, the buffering capacity of the calc-silicate rocks would have been completely exhausted and the grossular-rich garnet would have been completely consumed.

Overall, these results demonstrate that the studied calc-silicate rocks behaved as a closed system during their prograde and early-retrograde evolution, although their volume abundance within the hosting paragneiss is low: this is a common feature of many granulitic terrains (e.g. Gordon and Greenwood 1971; Buick et al. 1994; Harley et al. 1994; Bhowmik et al. 1995; Sengupta et al. 1997; Dasgupta and Pal 2005). It is worth noting that, at the *P–T* conditions corresponding to the garnet growth in the calc-silicate rocks, the hosting paragneiss experienced a significant degree of anatexis through muscovite and biotite de-hydration melting. H_2O released during this process was dissolved in the melt without formation of a vapour phase and therefore did not result in a significant fluid infiltration within the inter-layered metacarbonate rocks.

Origin of graphite

The systematic occurrence of large and abundant graphite flakes in layers A of both the samples suggests that graphite may have precipitated from the CO_2-rich C–O–H fluid internally produced through the garnet-forming reaction 24b. Graphite precipitates from a C–O–H fluid when the bulk composition of the fluid enters the field of graphite stability (Fig. 14). This may occur through two basic types of mechanisms (e.g. Ohmoto and Kerrick 1977; Frost 1979; Holloway 1984; Connolly and Cesare 1993; Connolly 1995; Luque et al. 1998; Pasteris 1999): (1) precipitation of graphite may be induced isochemically by a decrease in temperature and/or an increase in pressure, because the graphite stability field increases in size following either of those changes; (2) graphite precipitation may involve changing the composition of the fluid in order to bring the system into the graphite stability field at some *P* and *T*.

Cooling of C-bearing fluid is considered to be an effective mechanism for causing graphite precipitation. In the case of the studied samples, however, cooling is associated with decompression, and the contrasting effects of pressure decrease must be also considered. The graphite saturation curve in the ternary C–O–H diagram along a cooling and decompression path approximating that followed by the studied samples (Fig. 14) is only slightly shifted due to cooling and decompression; therefore in isolation, this mechanism is probably inadequate to explain the graphite in layer A.

Hydration reactions at constant *P* and *T* represent an efficient mechanism to change the composition of the fluid in an internally buffered system (i.e. without requiring the influx of external fluids). Hydration reactions can in fact deplete a fluid in H_2O, thereby enriching it in carbon causing graphite precipitation. The widespread occurrence of hydrated minerals (kaolinite, smectite and chlorite) replacing plagioclase and/or clinopyroxene in layers A (especially in sample 06-53) suggests that hydration reactions took place in the studied rocks. These observations suggest that precipitation of graphite was triggered by hydration reactions (Fig. 14).

If graphite was precipitated in a true closed system, then the amount of graphite should be directly related to the amount of decarbonation (i.e. to the amount of garnet formed through reaction 24b). Specifically, the observed garnet modes, 35 and 41 vol% (samples 06-53 and 06-57, respectively), would require graphite modes of 0.70 and

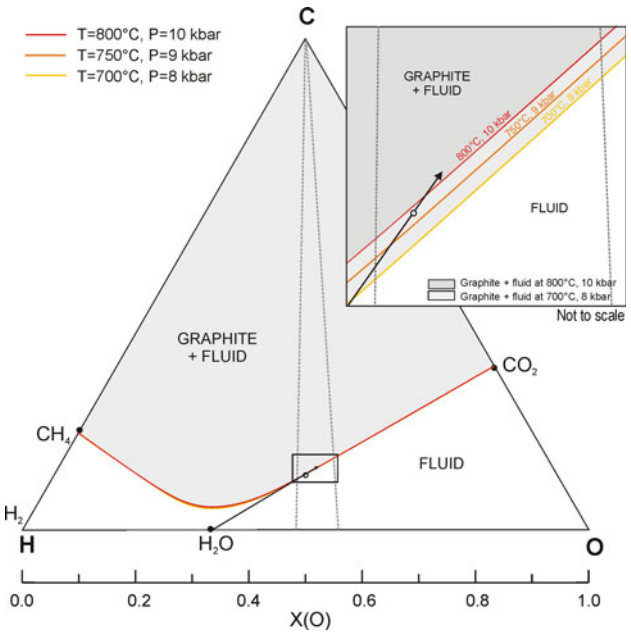

Fig. 14 Ternary C–O–H diagram and graphite saturation *curves* calculated at *P–T* conditions lying along the cooling and decompression path experienced by the studied calc-silicate rocks. The *shaded area* represents the fluid + graphite field, the area below the carbon saturation surface are carbon-undersaturated fluids. Carbon-saturated fluids with X_O close to 0 are CH_4 ($\pm H_2$)-rich, whereas fluids with X_O close to 1 are CO_2 ($\pm$CO)-rich. Pure H_2O fluid has $X_O = 1/3$. The *dashed tie lines* represent the fluid composition as constrained by the *P–T–X* grids (see discussion in the text): $0.30 < X(CO_2) < 0.44$ [i.e. $0.48 < X_O < 0.56$; $X_O = (X_{CO_2} + 1)/(3 - X_{CO_2})$: Connolly and Cesare 1993; Connolly 1995]. The *empty point* represents an hypothetical carbon-undersaturated C–O–H fluid at peak conditions (800 °C, 10 kbar; graphite saturation *curve* in *red*). This carbon-undersaturated fluid becomes carbon-saturated during cooling and decompression at 700 °C, 8 kbar (graphite saturation *curve* in *yellow*). Alternatively, H_2O depletion due to hydration reactions moves the fluid composition into the *shaded area* (see the *black arrow*) and graphite precipitates

0.82 vol%, respectively (Table 2). These graphite modes are comparable to those observed (ca. 1 vol%), suggesting that the studied calc-silicate rocks behaved as a closed system during their prograde and early-retrograde evolution.

Conclusions

The results of this study demonstrate that calc-silicate rocks of appropriate composition may act as CO_2 source during prograde heating and/or early decompression, releasing internal CO_2-rich fluids through garnet-forming reactions. However, if the system remains closed, fluid–rock interactions may induce hydration of the calc-silicate assemblages and the in situ graphite precipitation, thereby removing carbon from the fluids. The interplay between these two contrasting processes—i.e. production of metamorphic CO_2-rich fluids versus carbon sequestration through graphite precipitation—must be taken in account when dealing with a global estimate of the role exerted by decarbonation processes on the orogenic CO_2 cycle. In this framework, additional metamorphic CO_2-producing processes certainly exist (see Huizenga and Touret 2012 for a review), such as the Fe^{3+} reduction during biotite dehydration melting in graphitic metapelites (Cesare et al. 2005) and carbon oxidation in graphite-bearing sediments by H_2O derived from dehydration reactions (Touret 1971) or crystallizing granitic melts (Hollister 1988), and should be investigated as well.

Acknowledgments This study is part of the SHARE (Stations at High Altitude for Research on the Environment) Project, financially supported by the Ev-K2-CNR in collaboration with the Nepal Academy of Science and Technology as foreseen by the Memorandum of Understanding between Nepal and Italy, and thanks to contributions from the Italian National Research Council and the Italian Ministry of Foreign Affairs. Fieldwork was carried out thanks to financial support from the Italian National Research Council and PRIN 2006 (2006040882-003). Laboratory work was supported by PRIN 2011 (2010PMKZX7) and University of Torino—Call 1—Junior PI Grant (TO_Call1_2012_0068). FR and CG acknowledge B Lombardo for discussion in the field, and S Ferrando for constructive discussions about decarbonation processes and graphite precipitation. P. Sengupta and J. Touret are gratefully acknowledged for their inspiring and constructive reviews.

References

Abart R, Connolly JAD, Trommsdorff V (1992) Singular point analysis: construction of Schreinemakers projections for systems with a binary solution. Am J Sci 292:778–805

Ague JJ (2000) Release of CO_2 from carbonate rocks during regional metamorphism of lithologically heterogeneous crust. Geology 28:1123–1126

Baker J, Holland T, Powell R (1991) Isograds in internally buffered systems without solid solutions: principles and examples. Contrib Mineral Petrol 106:170–182

Berner RA (1999) A new look at the long-term carbon cycle. GSA Today 9(11):1–6

Berner RA, Lasaga AC (1989) Modeling the geochemical carbon cycle. Sci Am 260:74–81

Bhowmik SK, Dasgupta S, Hoernes S, Bhattacharya PK (1995) Extremely high-temperature calcareous granulites from the Eastern Ghats, India: evidence for isobaric cooling, fluid buffering and terminal channelized fluid flow. Eur J Mineral 7:689–703

Bickle MJ (1996) Metamorphic decarbonation, silicate weathering and the long-term carbon cycle. Terra Nova 8:270–276

Buick IS, Harley SL, Cartwright IC (1993) Granulite facies metasomatism: zoned calc-silicate boudins from the Rauer Group, East Antarctica. Contrib Mineral Petr 113:557–571

Buick IS, Cartwright I, Hand M, Powell R (1994) Evidence for pre-regional metamorphic fluid infiltration of the lower Calcsilicate Unit, Reynolds Range Group (central Australia). J Metamorph Geol 12:789–810

Buick IS, Cartwright I, Harley SL (1998) The retrograde P-T-t path for low-pressure granulites from the Reynolds Range, central Australia: petrological constraints and implications for low-P/high-T metamorphism. J Metamorph Geol 16:511–529

Carmichael DM (1991) Univariant mixed-volatile reactions: pressure–temperature phase diagrams and reaction isograds. Can Mineral 29:741–754

Castelli D, Rolfo F, Groppo C, Compagnoni R (2007) Impure marbles from the UHP Brossasco-Isasca Unit (Dora-Maira Massif, western Alps): evidence for Alpine equilibration in the diamond stability field and evaluation of the X(CO_2) fluid evolution. J Metamorph Geol 25:587–603

Cesare B, Meli S, Nodari L, Russo U (2005) Fe^{3+} reduction during biotite melting in graphitic metapelites: another origin of CO_2 in granulites. Contrib Mineral Petr 149:129–140

Connolly JAD (1990) Multivariable phase diagrams: an algorithm based on generalize thermodynamics. Am J Sci 290:666–718

Connolly JAD (1995) Phase diagram methods for graphitic rocks and application to the system C–O–H–FeO–TiO2–SiO2. Contrib Mineral Petr 119:94–116

Connolly JAD (2009) The geodynamic equation of state: what and how. Geochem Geophys Geosyst 10:Q10014

Connolly JAD, Cesare B (1993) C–O–H–S fluid compositions and oxygen fugacity in graphitic metapelites. J Metamorph Geol 11:379–388

Connolly JAD, Trommsdorff V (1991) Petrogenetic grids for metacarbonate rocks: pressure–temperature phase-diagrams for mixed-volatile systems. Contrib Mineral Petrol 108:93–105

Cossio R, Borghi A, Ruffini R (2002) Quantitative modal determination of geological samples based on X-ray multielemental map acquisition. Microsc Microanal 8:139–149

Dasgupta S (1993) Contrasting mineral parageneses in high temperature calc-silicate granulites: examples from the Eastern Ghats, India. J Metamorph Geol 11:193–202

Dasgupta S, Pal S (2005) Origin of grandite garnet in calc-silicate granulites: mineral–fluid equilibria and petrogenetic grids. J Petrol 46:1045–1076

Evans KA (2011) Metamorphic carbon fluxes: how much and how fast? Geology 39:95–96

Ferry JM (1983) Regional metamorphism of the Vassalboro Formation, south–central Maine, USA: a case study of the role of a fluid in metamorphic petrogenesis. J Geol Soc Lond 140:551–576

Fitzsimons ICW, Harley SL (1994) Garnet coronas in scapolite–wollastonite calc-silicates from East Antarctica: the applications

and limitations of activity corrected grids. J Metamorph Geol 12:761–777

Frost BR (1979) Mineral equilibria involving mixed-volatiles in a C–O–H fluid phase: the stabilities of graphite and siderite. Am J Sci 279:1033–1059

Gaillardet J, Galy A (2008) Himalaya-carbon sink or source? Science 320:1727–1728

Gordon TM, Greenwood HJ (1971) The stability of grossularite in H_2O–CO_2 mixtures. Am Mineral 56:1674–1688

Goscombe B, Gray D, Hand M (2006) Crustal architecture of the Himalayan metamorphic front in eastern Nepal. Gondwana Res 10:232–255

Groppo C, Rolfo F, Lombardo B (2009) P–T evolution across the Main Central Thrust Zone (Eastern Nepal): hidden discontinuities revealed by petrology. J Petrol 50:1149–1180

Groppo C, Rubatto D, Rolfo F, Lombardo B (2010) Early Oligocene partial melting in the Main Central Thrust Zone (Arun Valley, eastern Nepal Himalaya). Lithos 118:287–301

Groppo C, Rolfo F, Mosca P (2013) The cordierite-bearing anatectic rocks of the Higher Himalayan Crystallines (eastern Nepal): low-pressure anatexis, melt-productivity, melt loss and the preservation of cordierite. J Metamorph Geol 31:187–204

Harley SL, Buick IS (1992) Wollastonite–scapolite assemblages as indicators of granulite pressure–temperature–fluid histories: the Rauer Group, East Antarctica. J Petrol 33:693–728

Harley SL, Fitzsimons ICW, Buick IS (1994) Reactions and textures in wollastonite–scapolite granulites and their significance for pressure–temperature–fluid histories of high grade terranes. Precambrian Res 66:309–323

Holland TJB, Powell R (1998) An internally consistent thermodynamic data set for phases of petrologic interest. J Metamorph Geol 16:309–343

Hollister LS (1988) On the origin of CO_2-rich fluid inclusions in migmatites. J Metamorph Geol 6:467–474

Holloway JR (1984) Graphite–CH_4–H_2O–CO_2 equilibria at low-grade metamorphic conditions. Geology 12:455–458

Huizenga JM, Touret JLR (2012) Granulites, CO_2 and graphite. Gondwana Res 22:799–809

Kerrick DM (1974) Review of mixed-volatile (H_2O–CO_2) equilibria. Am Mineral 59:729–762

Kerrick DM, Caldeira K (1993) Paleoatmospheric consequences of CO_2 released during early Cenozoic regional metamorphism in the Tethyan orogen. Chem Geol 108:201–230

Luque FJ, Pasteris JD, Wopenka B, Rodas M, Barrenechea JF (1998) Natural fluid deposited graphite: mineralogical characteristics and mechanisms of formation. Am J Sci 298:471–498

Mosca P, Groppo C, Rolfo F (2011) Geological and structural architecture of the Kangchenjunga region in Eastern Nepal. J Nepal Geol Soc 43:1–12

Mosca P, Groppo C, Rolfo F (2012) Structural and metamorphic features of the Main Central Thrust Zone and its contiguous domains in the eastern Nepalese Himalaya. J Virtual Expl Electron Ed 41, paper 2

Ohmoto H, Kerrick D (1977) Devolatilization equilibria in graphitic systems. Am J Sci 277:1013–1044

Omori S, Liou JG, Zhang RY, Ogasawara Y (1998) Petrogenesis of impure dolomitic marble from the Dabie Mountains, central China. Isl Arc 7:98–114

Pasteris JD (1999) Causes of the uniformly high crystallinity of graphite in large epigenetic deposits. J Metamorph Geol 17:779–787

Pouchou JL, Pichoir F (1988) Determination of mass absorption coefficients for soft X-Rays by use of the electron microprobe. Microbeam Analysis, San Francisco Press, pp 319–324

Robinson P (1991) Eye of the petrographer, mind of the petrologist. Am Mineral 76:1781–1810

Searle MP, Law RD, Godin L et al (2008) Defining the Himalayan Main Central Thrust in Nepal. J Geol Soc Lond 165:523–534

Selverstone J, Gutzler DS (1993) Post-125 Ma carbon storage associated with continent–continent collision. Geology 21:885–888

Sengupta P, Raith MM (2002) Garnet stoichiometry as petrogenetic indicator: an example from the marble–calc-silicate interface from Kondapalle, Eastern Ghats Belt. Am J Sci 302:686–725

Sengupta P, Sanyal S, Dasgupta S, Fukuoka M, Ehl J, Pal S (1997) Controls of mineral reactions in high-grade garnet–wollastonite–scapolite-bearing calc-silicate rocks: an example from Anakapalle, Eastern Ghats, India. J Metamorph Geol 15:551–564

Skelton A (2011) Flux rates for water and carbon during greenschist facies metamorphism. Geology 39:43–46

Stephenson NCN, Cook NDJ (1997) Metamorphic evolution of calcsilicate granulites near Battye Glacier, northern Prince Charles Mountains, East Antarctica. J Metamorph Geol 15:361–378

Touret JLR (1971) Le faciès granulite en Norvège méridionale. II Les inclusions fluides. Lithos 4:423–436

Warren RG, Hensen BJ, Ryburn RJ (1987) Wollastonite and scapolite in Precambrian calc-silicate granulites from Australia and Antarctica. J Metamorph Geol 5:213–233